Atmospheric
Measurement
Techniques

A nonlinear data-driven approach to bias correction of XCO_2 for NASA's OCO-2 ACOS version 10

William R. Keely[1], **Steffen Mauceri**[2], **Sean Crowell**[3], **and Christopher W. O'Dell**[4]

[1]Data Science and Analytics Institute, University of Oklahoma, Norman, OK, USA
[2]Jet Propulsion Laboratory, California Institute of Technology, Pasadena, CA, USA
[3]School of Meteorology, University of Oklahoma, Norman, OK, USA
[4]Cooperative Institute for Research in the Atmosphere, Colorado State University, Fort Collins, CO, USA

Correspondence: William R. Keely (william.r.keely@ou.edu)

Abstract. Measurements of column-averaged dry air mole fraction of CO_2 (termed XCO_2) from the Orbiting Carbon Observatory-2 (OCO-2) contain systematic errors and regional-scale biases, often induced by forward model error or nonlinearity in the retrieval. Operationally, these biases are corrected for by a multiple linear regression model fit to co-retrieved variables that are highly correlated with XCO_2 error. The operational bias correction is fit in tandem with a hand-tuned quality filter which limits error variance and reduces the regime of interaction between state variables and error to one that is largely linear. While the operational correction and filter are successful in reducing biases in retrievals, they do not allow for throughput or correction of data in which biases become nonlinear in predictors or features. In this paper, we demonstrate a clear improvement in the reduction in error variance over the operational correction by using a set of nonlinear machine learning models, one for land and one for ocean soundings. We further illustrate how the operational quality filter can be relaxed when used in conjunction with a nonlinear bias correction, which allows for an increase in sounding throughput by 14 % while maintaining the residual error in the operational correction. The method can readily be applied to future Atmospheric CO_2 Observations from Space (ACOS) algorithm updates, to OCO-2's companion instrument OCO-3, and to other retrieved atmospheric state variables of interest.

1 Introduction

Carbon dioxide (CO_2) is a key contributor to radiative forcing, and hence rising levels in the atmosphere are of concern due to their influence on future climate. Following a long history of critical in situ measurements of CO_2 at key sites around the world that allowed us to better understand the carbon cycle on continental scales, the era of space-based remote sensing began with the Scanning Imaging Absorption Spectrometer for Atmospheric Chartography (SCIAMACHY) in March 2002 (Bovensmann et al., 1999) and the Atmospheric Infrared Sounder (AIRS) launched in May 2002 (Aumann et al., 2003). These missions were followed by dedicated CO_2 observers such as the Greenhouse gases Observing SATellite (GOSAT) mission in 2009 (Kuze et al., 2009) and the Orbiting Carbon Observatory-2 (OCO-2) in 2014 (Crisp et al., 2004). These data have yielded substantial scientific insights, such as a much more dynamic tropical carbon cycle compared with previous understanding (e.g., Liu et al., 2017; Palmer et al., 2019; Crowell et al., 2019; Peiro et al., 2022), as well as studies into power plant emissions and plumes (Nassar et al., 2017).

OCO-2 measures reflected solar radiances, from which column-averaged CO_2 dry air mole fractions (XCO_2) are retrieved with the NASA Atmospheric CO_2 Observations from Space (ACOS) algorithm (Crisp et al., 2012; O'Dell et al., 2012; Connor et al., 2008). Radiances are measured in the near-infrared oxygen A band near 0.76 µm, the shortwave infrared weak CO_2 band near 1.6 µm, and the shortwave infrared strong CO_2 band near 2.05 µm. ACOS is based on Bayesian optimal estimation (Rodgers, 2000) that adjusts

input parameters (e.g., XCO_2, aerosols, surface characteristics, surface pressure) to maximize agreement between a modeled spectrum (derived by a radiative transfer model) and OCO-2 measurements. The parameters that best explain the measured radiances are labeled as the "retrieved" parameters. ACOS has undergone continuous improvement since the initial version.

Since the radiances contain uncorrected calibration artifacts and the modeled representation of the atmospheric radiative transfer is not perfect, retrieved parameters contain systematic biases. The inverse problem is under-constrained and leads to posterior errors in retrieved parameters that are correlated. To correct for errors in XCO_2 arising from these types of dependencies, a multiple linear regression (MLR) bias correction with co-retrieved state variables or features used as predictors is fit to the difference (ΔXCO_2) between the ACOS-retrieved XCO_2 and a truth proxy estimate of XCO_2. This method was first introduced for ACOS retrievals applied to the GOSAT instrument (Wunch et al., 2011) and later extended to OCO-2 and OCO-3 (O'Dell et al., 2018; Taylor et al., 2020, 2023). The MLR bias correction is fit in tandem with a quality filter of empirically defined thresholds on a set of features. The bias correction and quality filter are derived iteratively, with filter thresholds chosen restricting features to a range in which the relationship between ΔXCO_2 and the parameters are mostly linear, improving the goodness of fit for the multilinear regression, which is then used in turn to retune the quality filter thresholds. The combined bias correction and quality filtering process is derived manually so that the final product must be hand-tuned for each algorithm update. After the feature-based correction, a footprint correction and global Total Carbon Column Observing Network (TCCON) offset are applied. The combined bias correction and quality filter process is robust across a set of ground truth proxy metrics and greatly reduces both mean bias and error scatter of XCO_2 retrieved from OCO-2. Full details of the operational bias correction and filtering can be found in O'Dell et al. (2018).

A drawback of applying the quality filter is the exclusion of data due to the linear assumption of the bias correction to which the quality filter limits the regime of interaction between state vector variables and ΔXCO_2, thus removing data where the bias is nonlinear. Due to loss of data, the bias correction and quality filter are often disregarded for local studies (Nassar et al., 2017; Mendonca et al., 2021) and are too limiting for certain regions (Jacobs et al., 2020). Applying nonlinear machine learning techniques has shown great promise for the task of bias correction for GOSAT and GOSAT-2 (Noël et al., 2022) and TROPOMI (Schneising et al., 2019). Specific correction of 3D cloud biases for OCO-2-retrieved XCO_2 (Massie et al., 2016) using a nonlinear method fit on a small set of features correlated with 3D cloud effects in addition to the linear operational correction is demonstrated in Mauceri et al. (2023).

This research demonstrates a general nonlinear bias correction approach for OCO-2 build 10 (B10; Taylor et al., 2023) via a machine learning method and provides a post hoc explanation of the overall contribution of the selected state vector features. Our nonlinear bias correction is shown to reduce systematic errors and increase the percentage of good-quality soundings by allowing for the relaxation of the hand-tuned thresholds employed with the standard quality threshold method. The framework presented in this paper for identifying informative features for bias correction can be adapted for future OCO-2 and 3 ACOS algorithm updates.

2 Data

To develop a bias correction, we define three truth proxy datasets for the true atmospheric column mole fraction. ΔXCO_2 is then set as the difference between the raw ACOS retrieval of XCO_2 and the truth proxy estimate of XCO_2, as shown in Eq. (1). For the TCCON and model mean truth proxies, the OCO-2 averaging kernel is also applied as described in Taylor et al. (2023).

$$\Delta XCO_2 = XCO_{2,ACOS} - XCO_{2,Proxy} \qquad (1)$$

We use the same proxy datasets used in the development of the operational bias correction (Osterman et al., 2020): co-located OCO-2 soundings with TCCON, a collection of small area clusters of soundings for which XCO_2 is not expected to vary above the instrument noise, and a set of modeled mole fractions whose underlying surface flux is constrained by the NOAA global in situ network (Masarie et al., 2014). Datasets include soundings from November 2014 through to February 2019. Each truth proxy captures a different scale of retrieval error and as such gives complementary information as described in O'Dell et al. (2018). All datasets were sampled in conjunction with corresponding locations and times in the OCO-2 B10 L2 Lite files which can be found at https://disc.gsfc.nasa.gov/datasets/ (last access: 10 January 2022). Spatial coverage and sounding count are shown in Fig. 1. The newest version available, the level 2 product, is build 11 (B11); however at the time of writing it was undergoing reprocessing.

2.1 TCCON truth proxy

TCCON is a system of ground-based sun-looking Fourier transform spectrometers with growing global coverage that retrieves column-averaged dry air mole measurements of the trace greenhouse gases from radiances in similar spectral bands to OCO-2. Since each site has been extensively validated against World Meteorological Organization (WMO)-traceable in situ observations on board aircraft, TCCON offers the most accurate comparison for XCO_2 (Wunch et al., 2010). While TCCON is well calibrated, site coverage is
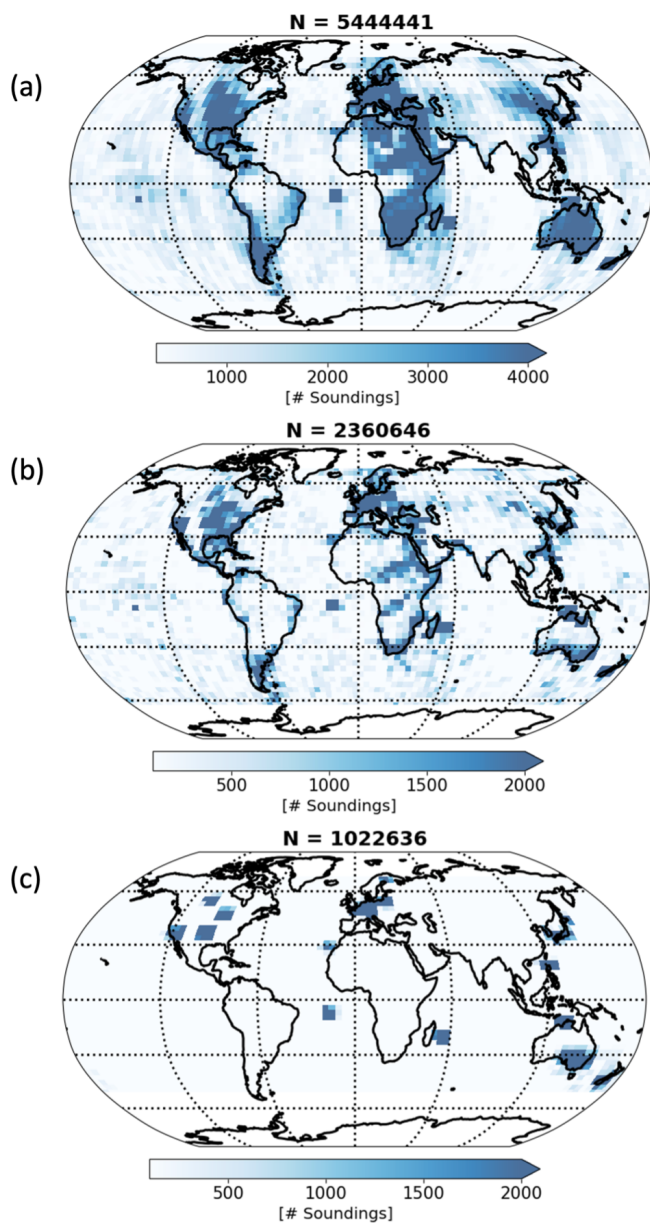
Figure 1. Spatial coverage for each truth proxy. The mean of a set of flux models is shown in panel **(a)**, small area approximation is shown in panel **(b)**, and TCCON is shown in panel **(c)**.

limited outside of North America, Europe, and Oceania. The TCCON dataset therefore is spatially the sparsest of the three truth proxies and offers non-uniform point comparisons. We use the same dataset as the operational correction consisting of OCO-2 soundings co-located with TCCON GGG2014 measurements (Wunch et al., 2017, 2011) in space ($2.5°$ lat, $5°$ long) and time (2 h). The stations used in this work are shown in Table 1.

2.2 Small area approximation truth proxy

The small area approximation described in O'Dell et al. (2018) offers insight into small-scale drivers of bias and retrieval variability. The small area approximation truth proxy assumes that XCO_2 within a 100 km neighborhood is largely uniform for a given overpass by OCO-2. This assumption is evaluated in Worden et al. (2017), where it was found by using a high-resolution atmospheric model (GEOS-5) that variance of XCO_2 is around 0.1 ppm per 100 km. The proxy offers improved spatial coverage compared to TCCON but struggles to capture biases with low variability over the small area.

2.3 Flux models truth proxy

A set of flux inversion models form the largest of the truth proxy datasets, both in number of soundings and in spatial coverage. The models included in this truth proxy set are found in Table 2. The posterior XCO_2 fields produced by the models are sampled along OCO-2 tracks; the proxy is then computed as the average of the models at every sounding where there is good agreement (within 1.5 ppm) among models (O'Dell et al., 2018; Osterman et al., 2020).

3 Methods

3.1 Gradient boosting

To model systematic error from co-retrieved state vector elements, we employ a machine learning method known as extreme gradient boosting or XGBoost (Chen and Guestrin, 2016) which can fit both linear and nonlinear relationships. XGBoost is an ensemble model where a set of simple models known as regression trees (Breiman 1984) are sequentially trained, with each new member fit on residuals of the previous trees. During inference, the weighted sum is taken across the ensemble members. Members are grown or fit by selecting features that provide high information gain (Eq. 2). Information gain is calculated by evaluating the sum of the gradients G and hessians H of the loss function at left and right leaf nodes when selecting split points for a feature during tree fitting. For our experiments we minimize the mean squared error between the truth proxy bias y_i and the estimate $\hat{y}_i$ as the loss function, as shown in Eq. (3). Features that are informative for reducing residual error during tree development yield high gain values. These values can be summed across trees in the ensemble to produce a ranking of feature contribution. This provides a post hoc method of interpretability yielding a high level or global view of feature importance to correcting ΔXCO_2. While this method of interpretability is less informative than the regression coefficients provided by a linear model, it is useful for tasks such as feature selection.

XGBoost employs L_1 and L_2 norm regularization to reduce overfitting to outliers present in the training dataset. The

Table 1. TCCON sites used in bias correction and filtering for B10 ACOS.

TCCON (station name* means an island)	Continent	Latitude	Altitude (m)	Operational date range	Data citation
Saga*	Asia	33.2° N	7	June 2011–present	Shiomi et al. (2014)
Orléans	Europe	48.0° N	130	August 2009–present	Warneke et al. (2019)
Garmisch	Europe	47.5° N	740	July 2007–present	Sussman and Rettinger (2018)
Tsukuba*	Asia	36.1° N	30	December 2008–present	Morino et al. (2018a)
Sodankylä	Europe	67.4° N	188	January 2009–present	Kivi et al. (2014)
Rikubetsu	Asia	43.5° N	380	November 2013–present	Morino et al. (2018c)
Izaña*	Africa	28.3° N	2367	May 2007–present	Blumenstock et al. (2017)
JPL	N. America	34.2° N	390	March 2011–July 2013 June 2017–May 2018	Wennberg et al. (2017a)
Bialystok	Europe	53.2° N	180	March 2009–October 2018	Deutscher et al. (2019)
Bremen	Europe	53.1° N	27	July 2004–present	Notholt et al. (2019)
Wollongong	Australia	34.4° S	30	May 2008–present	Griffith et al. (2014b)
Park Falls	N. America	45.9° N	440	May 2004–present	Wennberg et al. (2017b)
Réunion*	Africa	20.9° S	87	September 2011–present	De Maziére et al. (2017)
Anmyeondo	Asia	36.5° N	30	August 2014–present	Goo et al. (2014)
Darwin	Australia	12.4° S	30	August 2005–present	Griffith et al. (2014a)
Lauder*	Australia	45.0° S	370	June 2004–present	Pollard et al. (2019)
Lamont	N. America	36.6° N	320	July 2008–present	Wennberg et al. (2016)
Karlsruhe	Europe	49.1° N	116	September 2009–present	Hase et al. (2015)
Manaus	S. America	3.2° S	49.2	August 2014–June 2015	Dubey et al. (2014)
Paris	Europe	48.8° N	60	September 2014–present	Té et al. (2014)
Burgos*	Asia	18.5° N	35	March 2017–present	Morino et al. (2018b)

Table 2. Flux models used for the model mean truth proxy. TM5 – Global Chemistry Transport Model Transport Model 5; TM3 – Global Chemistry Transport Model Transport Model 3; LMDZ – Laboratoire de Météorology, EnKF – ensemble Kalman filter; 4D-Var – 4D-Variation Data Assimilation.

Model name	Institute	Transport model	Resolution (lat × long × time)	Inverse method	Citation
CarbonTracker	NOAA Global Monitoring Laboratory	TM5	2° × 3° × 3 h	EnKF	Peters et al. (2007), CarbonTracker (2021)
CarboScope	Max Planck Institute for Biogeochemistry	TM3	4° × 5° × 6 h	4D-Var	Rödenbeck (2005), Rödenbeck et al. (2018), CarboScope (2021)
CAMS	Copernicus Atmosphere Monitoring Service	LMDZ	1.9° × 3.75° × 3 h	4D-Var	Chevallier et al. (2010), CAMS (2021)

effect of the regularization is governed by the hyperparameters λ and γ and must be carefully selected or tuned. To find these hyperparameters we use a k-fold cross validation strategy in which the training dataset is divided into k subsets (we use $k = 10$) and each subset is sequentially held out for evaluation for a model trained on the rest of the data. Performance across the k folds is averaged, and the process is repeated for each potential selection of hyperparameters. We found a $\lambda_{\text{LAND}} = 2.5$ and $\gamma_{\text{LAND}} = 3.75$ for the land correction and $\lambda_{\text{OCEAN}} = 2.0$ and $\gamma_{\text{OCEAN}} = 10.0$.

$$\text{Information gain} = \frac{1}{2}\left[\frac{G_{\text{Left}}^2}{H_{\text{Left}} + \lambda} + \frac{G_{\text{Right}}^2}{H_{\text{Right}} + \lambda} - \frac{(G_{\text{Left}} + G_{\text{Right}})^2}{H_{\text{Left}} + H_{\text{Right}} + \lambda}\right] - \gamma \tag{2}$$

$$\text{Mean squared error loss} = \frac{1}{N}\sum_{i=1}^{N}(y_i - \hat{y}_i)^2 \tag{3}$$

3.2 Quality filtering

Soundings of the lowest quality are typically caught by the O$_2$ A band preprocessor (Taylor et al., 2012) and IMAP-DOAS (Frankenberg et al., 2005) algorithms due to clouds and low SNR in the continuum and are then screened out before being run through the L2 retrieval algorithm (Taylor et al., 2016). After retrieval, an additional number of soundings are flagged and removed for which the ACOS algorithm failed to converge or for which the chi-squared difference between modeled and measured spectra is too large. Additionally, large unphysical outliers present in the tails of the conditional distributions of several atmospheric state variables are also removed by hand using domain-expert-selected thresholds. Finally, users can select for high-quality retrievals using the binary XCO$_2$ quality flag (QF) with "good" data having a QF $= 0$ and "poor" data having QF $= 1$. The operational XCO$_2$ quality flag is derived using a set of filters applied to the state vector variables found in conjunction with linear parametric bias correction. An initial linear correction is fit on soundings that have passed the preprocessing filtering steps. Each filter is then hand selected, QF $= 1$ data are removed, and the bias correction is re-fit until a final set of filters and linear model weights are derived that sufficiently reduce mean bias and scatter (O'Dell et al., 2018).

To assess the ability of the nonlinear method to correct QF $= 1$ data and the potential for increased throughput of well-corrected data, we derive a new quality flag (QFNew). Our flag is developed in a similar fashion to the B10 quality flag for use with the nonlinear correction. The first step is to start with the same set of state vector variables and associated thresholds. Next, thresholds are relaxed for a selection of state vector variables that allow for higher sounding throughput while maintaining or reducing corrected ΔXCO$_2$ across truth proxies. Thresholds are never set to be more constrain-

ing than the B10 values in order to not remove soundings that are already considered to be of passing quality.

3.3 Training and test split

For training and evaluating the nonlinear correction, we subset each of our truth proxy datasets into training and testing datasets. First, datasets are split by the two surface types: ocean and land. In B10, both operation modes (nadir and glint) are combined for the land bias correction due to low variance in feature importance between nadir and glint (O'Dell et al., 2018). To compare to the operational correction, we also combine both modes for the land correction model. The land and ocean datasets are subset once more by truth proxy to identify informative features for the final land and ocean models. To ensure that model performance is indicative of how well the models generalize to unseen data, we hold out a year of data for evaluation of the final land model and ocean model. Models are trained on data from 2014, 2015, 2016, and 2017 and then evaluated on data from 2018. Since data from 2019 are limited, we exclude them from both training and evaluation.

3.4 Experiment design

First, the footprint correction as described in O'Dell et al. (2018) is applied to the training and evaluation datasets. We then evaluate two methods for bias-correcting retrieved XCO$_2$: a nonlinear machine learning model called XGBoost and, as a baseline, an MLR model trained similar to the hand-tuned model used in the operational correction. For correcting land nadir and land glint data, a single XGBoost model and MLR are trained using all three truth proxies. The predictor variables or features are the same for both model types. This allows for comparison between the nonlinear model and baseline linear method to properly assess that improved fit is coming from the captured nonlinearity and not just the inclusion of the additional predictors. A single XGBoost and MLR are derived for correcting ocean glint data, again using all three proxies and the same set of ocean features. We also compare our approach to the operational land correction and ocean correction for B10.

To identify a set of informative features to be used as inputs for the XGBoost land and ocean models, we first train a set of models independently on each truth proxy. These six models (three for land and three for ocean) are initially fit on a large set of potentially informative features, using QF $= 0 + 1$ data. The resulting feature importance derived from these initial models is used to filter down the feature set to identify a subset of features that is highly informative across truth proxies. The resulting feature sets are combined to train the final proposed model pair (one for land and one for ocean), which are trained using all truth proxies.

Next, we compare the final models trained on QF $= 0 + 1$ data against models trained only on good-quality data as-

signed $QF = 0$ and then evaluate each model pair on $QF = 0$ soundings that have been temporally held out. This is to ensure the ability of the nonlinear method to reproduce the linear model, which is the currently accepted community standard. Secondly, we evaluate the model trained on $QF = 0 + 1$ data on the excluded regime of data labeled $QF = 1$, where nonlinear relationships between ΔXCO_2 and predictors become more pronounced. Finally, we derive a new quality flag (QFNew) used in conjunction with the nonlinear correction that increases the throughput of well-corrected data while maintaining similar error metrics as the operational filter and correction.

4 Results

4.1 Feature selection

We select informative features for our bias correction following an iterative procedure. In the first step, we train XGBoost models for each proxy by surface type and operation mode (six models in total). These initial models are trained using a large subset of co-retrieved state vector variables (shown in Table C1) which are potentially informative for correcting ΔXCO_2 from the B10 L2 Lite files. The resulting models are used to rank features according to their information gain, which is defined in Eq. (2). Features that are less informative are removed from the set, and new models are trained with the reduced feature set. Afterwards, feature importance is once again evaluated. To ensure robustness to correlation among features (which information gain does not account for), we calculate Pearson's correlation values between features. Features with an absolute Pearson value greater than 0.5 are included one a time, and the feature with the highest importance is kept. This process is iteratively repeated until reaching a relatively small subset of maximally informative features. These features are combined to train the final bias correction models, which are trained on all proxies. Seven features are selected for land correction and five features for ocean, as shown in Fig. 2. The resulting features used in the final models and a brief description are shown in Table 3.

Features used for the operational correction are also highly informative for the proposed nonlinear corrections and include the difference between the retrieved CO_2 profile and prior profile used for land and ocean (co2_grad_del), as well as two surface pressure difference terms: dpfrac for land and dp_sco2 for ocean (Kiel et al., 2019). The co2_grad_del is the change in profile shape and the prior and is calculated as the difference in dry air mole fraction at the surface, denoted as $CO_2(1)$, from the fraction at ~ 0.6316 times the retrieved surface pressure; it is in units of parts per million (ppm). The calculation for co2_grad_del is shown in Eq. (4). For land, the dpfrac term is a difference ratio that considers the smaller dry air column over higher elevations and is defined in Eq. (5), where $X_{CO2,raw}$ is the uncorrected retrieval

of the column average and $P_{ap,SCO2}$ and P_{ret} are the prior surface pressure at the strong band pointing offset and retrieved pressure, respectively. For ocean, dp_sco2 is used and is the retrieved surface pressure minus the strong band prior. The extensive use of co2_grad_del and surface pressure deltas for bias correction is discussed in Kulawik et al. (2019).

$$\text{co2\_grad\_del} = \left[CO_{2,ret}(1) - CO_{2,ret}(0.6316) \right] \\ - \left[CO_{2,prior}(1) - CO_{2,prior}(0.6316) \right] \quad (4)$$

$$\text{dpfrac} = X_{CO2,raw} \left(1 - \frac{P_{ap,SCO2}}{P_{ret}} \right) \quad (5)$$

For land, the h2o_ratio is used and is the ratio of XH_2O estimated by single-band retrievals from the strong and weak CO_2 bands separately using the IMAP-DOAS algorithm, which can differ from unity in the presence of atmospheric scattering (Taylor et al., 2016). We use three aerosol features for our bias correction over land scenes, the first being the sum of dust, water, and sea salt optical thickness termed DWS. We include retrieved ice particle optical depth (aod_ice) and the finer stratospheric aerosol optical depth (aod_strataer). The last feature used for land, as well as for ocean, is the albedo slope for the strong CO_2 band termed albedo_slope_sco2. This variable represents the slope of the reflectance across the strong CO_2 spectral band for land soundings and the slope of the Lambertian component of the combined Cox–Munk and Lambertian Bidirectional Reflectance Distribution Function (BRDF) for ocean soundings (Cox and Munk, 1954). In addition to the co2_grad_del, albedo_slope_sco2, and dp_sco2, two additional variables are used for the correction of ocean G (glint) scenes. These are snr_wco2, which is the estimated signal-to-noise ratio derived during optimal estimation, and finally rms_rel_wco2, which is the percent residual error from the forward-modeled radiance for the weak CO_2 to the measured radiance.

4.2 Model evaluation for $QF = 0$

To ensure that the nonlinear method generalizes the linear relationships largely observed for $QF = 0$, we evaluate two XGBoost models – one which is fit on $QF = 0 + 1$ and one fit on $QF = 0$ – to an MLR fit on the same feature set as the nonlinear models. As the operational quality flag is hand-tuned by re-fitting an MLR, the regime between the variables selected for correction and systematic error are reduced to mostly linear relationships. The nonlinear method has only a marginal improvement over the MLR and B10 correction on soundings that are passed by the operational quality filter over land (0.02–0.04 ppm) and a slightly more substantial improvement over ocean (0.09–0.10 ppm) on the evaluation data. We found that retraining the XGBoost models on $QF = 0$ data does not offer a substantial reduction in error despite initial XGBoost models being trained on unfiltered data. We forgo the iterative refitting approach that is required for the MLR and operational correction by training
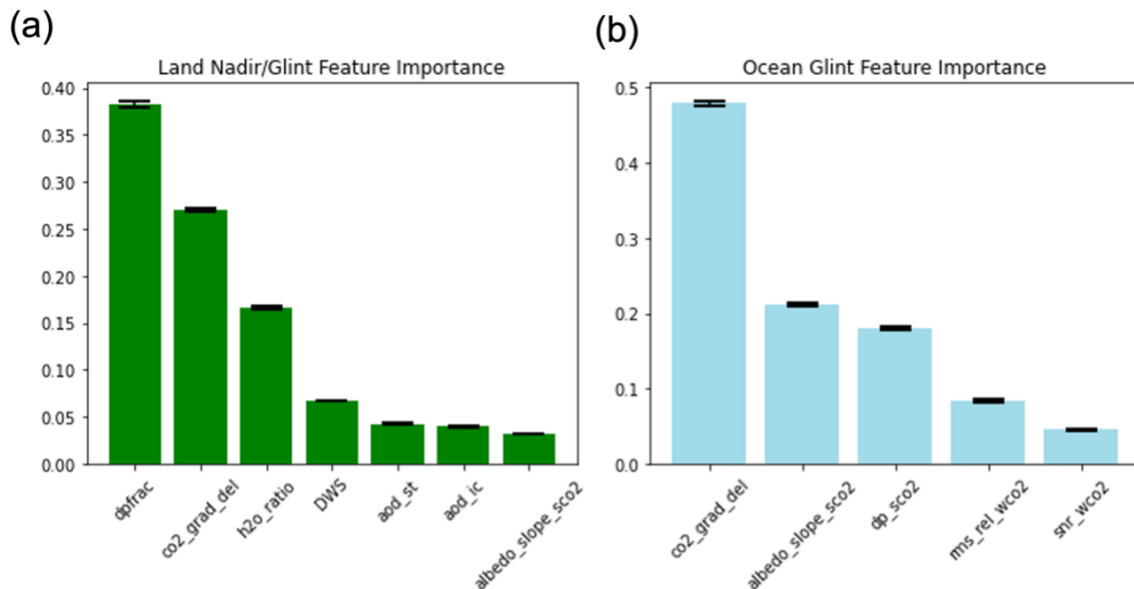
Figure 2. Feature importance for final land model trained with all proxies **(a)**. Feature importance for final ocean model trained with all proxies **(b)**. Error bars denote variance in feature importance across 10 runs with different random seeds.

Table 3. Selected features for use in our bias correction models. The first column shows state vector variable names as defined in the B10 L2 files, the second provides a brief description, and the last column shows which region and viewing mode correction the variable is used for. NG signifies nadir plus glint and G glint.

State variable	Description	Surface type and operation mode
dpfrac	Surface pressure difference that considers smaller dry air columns over higher elevations (Kiel et al., 2019).	Land NG
h2o_ratio	Ratio of retrieved H_2O column in weak and strong CO_2 bands by IMAP-DOAS.	Land NG
DWS	Additive combination of retrieved dust, water, and sea salt aerosol optical depth.	Land NG
aod_strataer (aod_st)	Retrieved upper-tropospheric plus stratospheric aerosol optical depth at $0.755\,\mu m$.	Land NG
aod_ice (aod_ic)	Retrieved ice cloud optical depth at $0.755\,\mu m$.	Land NG
co2_grad_del	Difference between the retrieved vertical CO_2 profile and prior.	Land NG/ocean G
albedo_slope_sco2	Retrieved strong band reflectance slope (land) or slope of Lambertian albedo component of BRDF (ocean).	Land NG/ocean G
dp_sco2	Surface pressure difference between the retrieved and prior, evaluated for the strong CO_2 band location on the ground.	Ocean G
rms_rel_wco2	RMSE of the L2 fit residuals in the weak CO_2 band relative to the signal.	Ocean G
snr_wco2	The estimated signal-to-noise ratio in the continuum of the weak CO_2 band.	Ocean G

once on $QF = 0 + 1$ data. Table 4 shows the $QF = 0$ RMSE results for XGBoost models trained on both $QF = 0 + 1$ data and $QF = 0$ data, alongside the MLR model fit to the filtered regime for 2018 and B10 operational correction.

4.3 Correcting outside of the filtered regime

Correction of systematic error outside of the quality-filtered regime ($QF = 1$) is difficult to fit with a linear model. Strong nonlinearities are observed for many of the co-retrieved state vector variables and ΔXCO_2. For many variables this behavior is observed over un-physical values in a few spurious

Table 4. RMSE scores for 2018 on $QF = 0$ data. Results are shown for land and ocean data by truth proxy and model. Two XGBoost models are shown: one trained on $QF = 0 + 1$ ($XGBoost_{QF0+1}$) data and then evaluated on $QF = 0$ and another ($XGBoost_{QF=0}$) trained and evaluated on only $QF = 0$ data. A multiple linear regression ($MLR_{QF=0}$) is also fit for $QF = 0$ using the same feature set. In the last column, RMSE for operationally corrected XCO_2 (B10) is shown.

Land $QF = 0$				
Truth proxy	$XGBoost_{QF=0+1}$ RMSE (ppm)	$XGBoost_{QF=0}$ RMSE (ppm)	$MLR_{QF=0}$ RMSE (ppm)	B10 RMSE (ppm)
Small area	0.83	0.82	0.84	0.85
TCCON	1.15	1.14	1.19	1.20
Model mean	1.05	1.05	1.09	1.11
All	1.03	1.02	1.05	1.07
Ocean $QF = 0$				
Truth proxy	$XGBoost_{QF=0+1}$ RMSE (ppm)	$XGBoost_{QF=0}$ RMSE (ppm)	$MLR_{QF=0}$ RMSE (ppm)	B10 RMSE (ppm)
Small area	0.45	0.44	0.56	0.52
TCCON	0.83	0.81	0.89	0.95
Model mean	0.67	0.66	0.78	0.76
All	0.65	0.65	0.75	0.74

soundings that are easily filtered out. Variables such as h2o_ratio which are responsible for the bulk of the quality filtering (h2o_ratio thresholds remove $\sim 10\%$ of soundings) exhibit such nonlinear characteristics over their marginal distributions. The dependent linear correction and quality filter is prohibitive for correcting and passing data in these regions of the domain. Figures 3 and 4 illustrate the interaction between state variables chosen for correction and ΔXCO_2. The nonlinear model (green) improves both the mean and variance of ΔXCO_2 over both the raw ΔXCO_2 (red) before correction and B10 correction (blue). Table 5 displays the RMSE scores of the XGBoost-corrected XCO_2 and operationally corrected XCO_2 for $QF = 1$ data. The nonlinear correction provides a large improvement in reducing the residual error for $QF = 1$ data over the operational correction with a 1.33–2.26 ppm improvement for land data and 1.11–1.38 ppm for ocean. These errors are still significantly larger than the corresponding $QF = 0$ errors.

4.4 Comparison to B10

For the operational correction, regression weights for the linear model are hand-selected that have good agreement in their correction across truth proxies. The full operational correction also includes a fixed correction for each of OCO-2's eight footprints, as described in Osterman et al. (2020). To provide a fair comparison between the full correction models, we also apply the footprint correction after applying the nonlinear feature correction. Table 6 shows the mean and 1σ standard deviation for each bias correction and QF regime. The largest improvement in the nonlinear method over B10 comes when correcting $QF = 1$ data, achieving a 59 % improvement in the reduction of error variance for land and a

Table 5. RMSE scores for 2018 on $QF = 1$ data. XGBoost-corrected XCO_2 and operationally corrected XCO_2 (B10) for land and ocean data.

Land $QF = 1$		
Truth proxy	$XGBoost_{QF=0+1}$ RMSE (ppm)	B10 RMSE (ppm)
Small area	1.92	3.25
TCCON	2.81	5.07
Model mean	2.46	3.95
Ocean $QF = 1$		
Truth proxy	$XGBoost_{QF=0+1}$ RMSE (ppm)	B10 RMSE (ppm)
Small area	1.25	2.36
TCCON	1.68	2.90
Model mean	1.53	2.91

67 % improvement for ocean data. The improvement in correction over B10 is less significant for $QF = 0$ with improvement of 8 % for land and 19 % for ocean.

Regionally, the nonlinear correction shows up to a 0.5 ppm improvement over northern Africa, where the B10 correction appears to underestimate ΔXCO_2 in comparison. A reduction in biases is also observed in large parts of South America's tropical and subtropical regions, as well as parts of tropical Asia shown in Fig. 5a. These regions also contain the largest difference in land NG (nadir plus glint) correction between the methods with an average difference (B10 − XGBoost) of −0.5 ppm. There is a slight positive difference between methods over the Amazon Basin and Congo
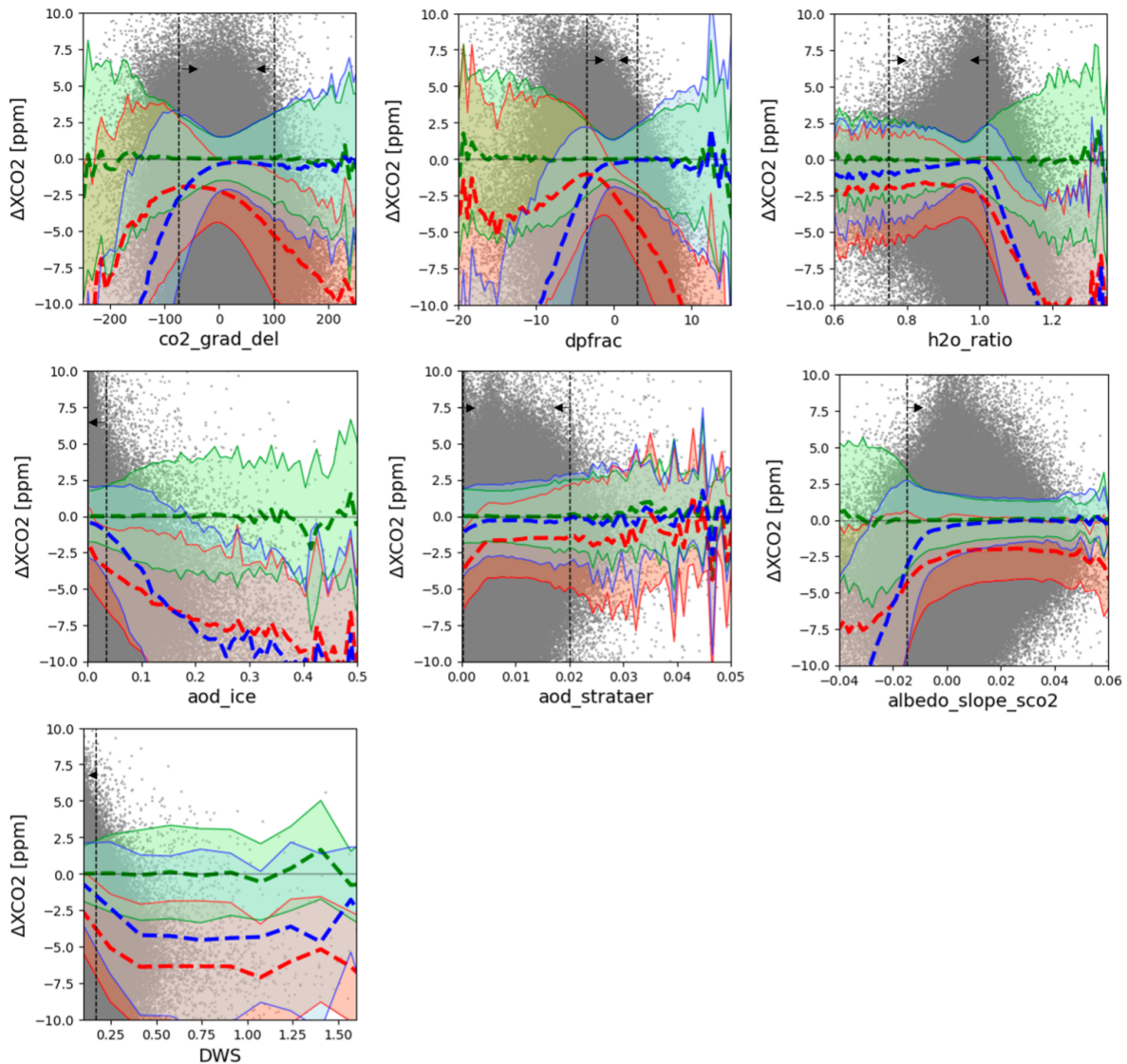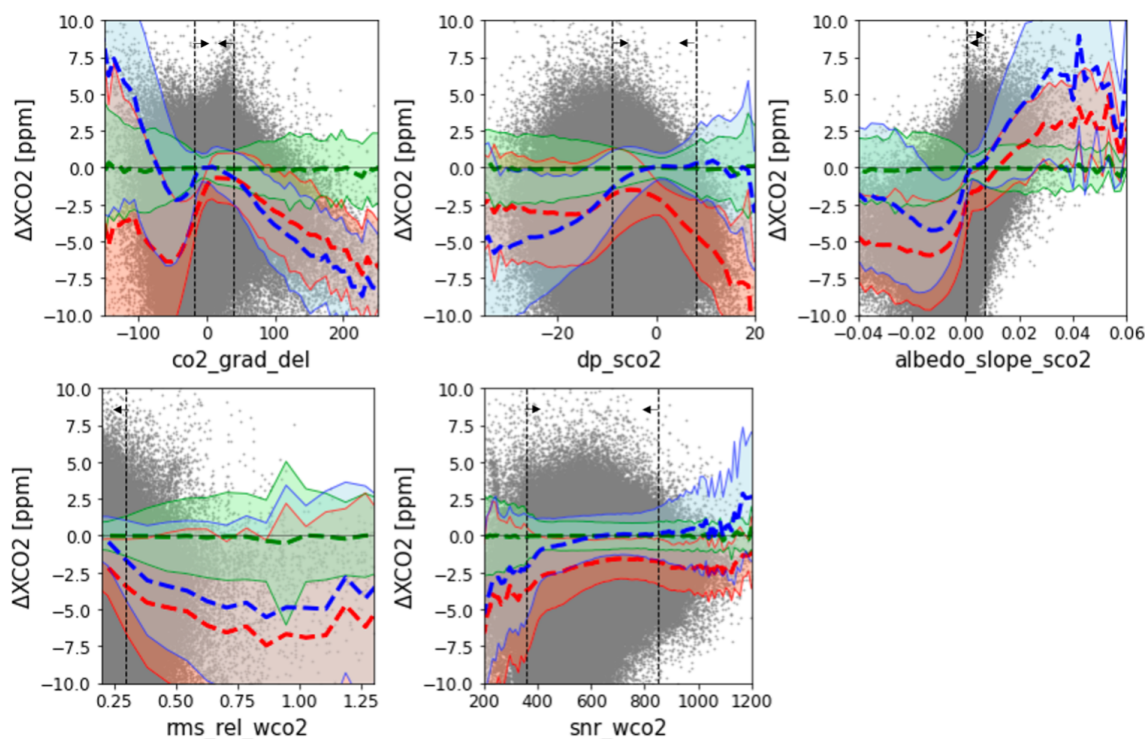
Figure 3. ΔXCO_2 vs. land features for 2018. Mean interaction and 2σ SD for uncorrected ΔXCO_2 plotted in red, XGBoost corrected in green, and B10 corrected in blue. The vertical black dotted lines indicate B10 QF filters, and arrows point towards the region assigned QF = 0. Individual soundings are shown with gray scatter.

rainforest (Fig. 5e). Figure 5c and d illustrate the improvement of the nonlinear method to correct QF = 1 data over the operational approach. For QF = 1, where the interaction between features and error is nonlinear, large biases in XCO_2 remain after operational correction. The XGBoost model reduces these remaining biases in many regions, indicating that there may still be usable data that are filtered out by the operational QF when paired with the nonlinear correction.

4.5 Increased sounding throughput

One of the benefits of the nonlinear bias correction is the potential for increased throughput of well-corrected QF = 1 data. Improved throughput of well-corrected data would be

of benefit to point analysis studies where data are limited by the operational QF and potentially of benefit to flux models as well. To provide an empirical example of this, we create a modified version of the operational XCO_2 quality flag utilizing our proposed ocean correction model and land correction model. We take a conservative approach where initial filter values are set equal to those of the operational quality filtering. Then, we select a few variables for which the filters are relaxed to increase sounding throughput while maintaining the RMSE of the combined operational correction and quality filter. With our new quality flag (QFNew), we are able to increase sounding throughput by approximately 14 % over the B10 QF while matching the RMSE of the B10 correction, as shown in Table 7.

Figure 4. ΔXCO_2 vs. ocean features for 2018. Mean interaction and 2σ SD for uncorrected ΔXCO_2 plotted in red, XGBoost corrected in green, and B10 corrected in blue. The vertical black dotted lines indicate B10 QF filters, and arrows point towards the region assigned $QF = 0$. Individual soundings are shown with gray scatter.

Table 6. Comparison of combined proxy mean and standard deviation XGBoost-corrected XCO_2, XCO_2 after the operational correction (B10), and un-corrected XCO_2 (raw) for 2018 and all QF filter regimes for both land and ocean data.

$QF = 0$			
Surface and mode	XGBoost (ppm)	B10 (ppm)	Raw (ppm)
Land NG	-0.04 ± 1.02	-0.13 ± 1.06	-1.90 ± 1.68
Ocean G	0.02 ± 0.64	0.18 ± 0.71	-1.61 ± 1.10
$QF = 1$			
Surface and mode	XGBoost (ppm)	B10 (ppm)	Raw (ppm)
Land NG	0.01 ± 2.45	-1.24 ± 3.83	-2.83 ± 3.69
Ocean G	-0.06 ± 1.50	-1.17 ± 2.59	-2.79 ± 2.75
$QF = 0 + 1$			
Surface and mode	XGBoost (ppm)	B10 (ppm)	Raw (ppm)
Land NG	-0.03 ± 1.75	-0.59 ± 2.64	-2.78 ± 2.73
Ocean G	-0.01 ± 1.07	-0.36 ± 1.85	-2.09 ± 2.03

For many features, the quality filters were not changed from the operational filters, as relaxing filters on variables that are already passing most of their conditional distributions would allow for only marginal improvements in throughput at the cost of large systematic errors. Therefore, we select only features for which large portions of the marginal distributions are removed by the operational flag and where the nonlinear correction improves both the mean and variance of ΔXCO_2. The relaxed filters for these variables are shown in Figs. B1 and B2 by the vertical red dashed lines, and the range of data assigned $QFNew = 0$ is shown in the red parentheses. The operational filter also minimizes the unitless metric of the binned standard deviation of ΔXCO_2 divided by the posterior XCO_2 uncertainty below a value of $3\,\mathrm{ppm\,ppm}^{-1}$ (Osterman et al., 2020). When tuning QFNew, we also aim to minimize this metric. Higher throughput of well-corrected data is observed in northern and central Africa, the Amazon Basin, and in latitudes above $60°$ N as seen in Fig. 6. While the selection of these variables and the relaxation of their filter values are subjective, this empirical result illustrates the benefit of a quality flag derived in conjunction with the nonlinear bias correction. Future work will focus on the automation of defining the quality flag thresholds using a data-driven approach.
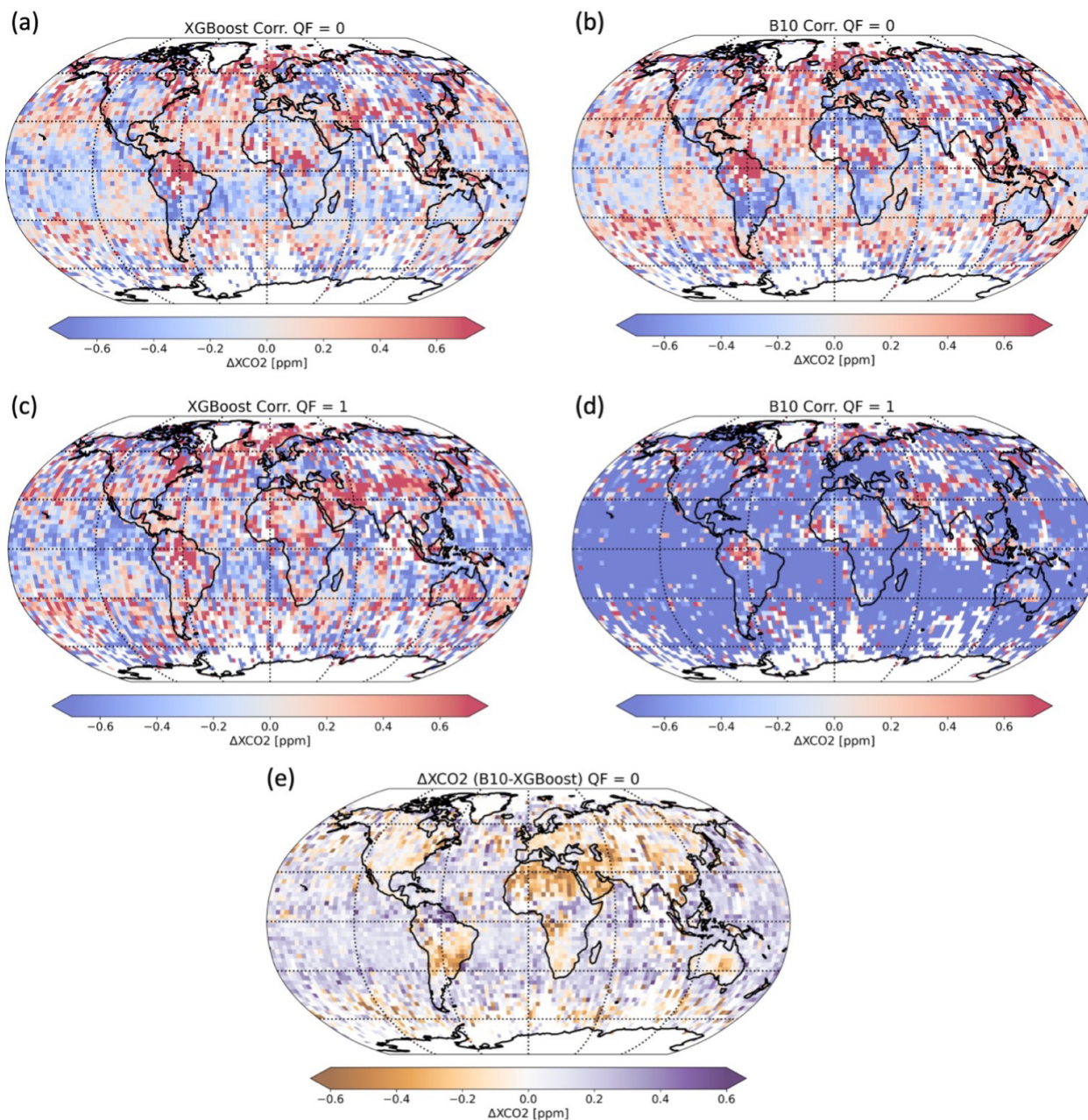
Figure 5. Remaining XCO$_2$ biases (ΔXCO$_2$) after correction for 2018 and model mean proxy, binned to a $3° \times 3°$ resolution. ΔXCO$_2$ after the XGBoost correction for QF $= 0$ is shown in panel (**a**), ΔXCO$_2$ after the B10 correction for QF $= 0$ is shown in panel (**b**), ΔXCO$_2$ after the XGBoost correction for QF $= 1$ is shown in panel (**c**), ΔXCO$_2$ after the B10 correction for QF $= 1$ is shown in panel (**d**), and the difference (B10 $-$ XGBoost) for QF $= 0$ is shown in panel (**e**).

Table 7. RMSE for combined XGBoost correction, B10 QF percent data throughput, and QFNew percent data throughput by surface and mode for 2018.

Surface (mode)	XGBoost RMSE (ppm)	B10 % passing (%)	QFNew % passing (%)
Land (nadir plus glint)	1.07	59	69
Ocean (glint)	0.72	60	74
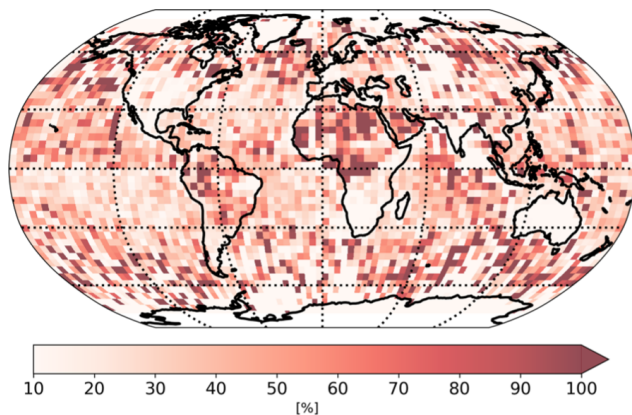
Figure 6. Relative increase in percent passing QFNew over B10 QF for 2018 aggregated by $4° \times 4°$ bins.

5 Discussion and future work

5.1 Generalization across proxies

We acknowledge that even with a temporal training and testing split, there is still some circularity due to the lack of a truly independent truth proxy. This issue has been discussed at length for the operational bias correction in Taylor et al. (2023), and the comparison and selection of independent validation datasets are still an open area of study. The risk of overfitting due to circularity becomes greater when fitting a more complex machine learning model. To evaluate generalizability to a fully independent validation proxy, we fit a set of XGBoost models on two truth proxies and evaluate on the third proxy which is held out during training. The same temporal split is used where 2018 data for the held-out proxy are used for evaluation. Results are shown in Fig. 7, for land, and Fig. 8, for ocean. Each column shows the residual fit for the hold-out proxy for QF = 0 (top row) and QF = 1 (bottom row). For QF = 0, increase in RMSE was minimal for both surface types and across proxies. There was some impact to performance on QF = 1 data when compared to training with all three proxies, particularly for TCCON with an increase in RMSE of ~ 0.1 ppm for land and ocean data, indicating that the information contained in TCCON is not adequately represented by the model mean and small area approximation proxies which capture variability at larger scales. A potential approach to reducing circularity in the evaluation of the truth proxies would be to train the bias correction on TCCON and either the model mean or small area approximation using the third proxy not chosen for validation.

5.2 Evaluating feature importance between filter regimes

To understand the contribution of the features to correcting bias in QF = 0 and QF = 1 data, we compare the information gain between the two regimes. To perform the ablation

study, we again employ the models trained on individual truth proxies and retrain and evaluate them on QF = 0 and again on QF = 1 data. Figure 9 shows the information gain for each filter regime for land and for ocean. For land, dpfrac and co2_grad_del are highly informative for correction of QF = 0 data by the machine learning model. Similarly for ocean QF = 0 data, the surface pressure delta term dp_sco2 and co2_grad_del are also highly informative. In operation, these terms are also used for bias correction in all ACOS versions (dpfrac replaced dP in build 9, B9) to date. These variables are responsible for the largest reduction in unexplained variance in the filtered regime (Payne et al., 2022; Osterman et al., 2020; O'Dell et al., 2018).

For land QF = 1 data, there are a drop in importance for co2_grad_del and dpfrac, a large increase for h2o_ratio, and relative increases for the albedo and aerosol terms. To explain the high importance for the h2o_ratio, we look to the nonlinear interaction outside of the bound imposed by the operational filter which removes soundings with a h2o_ratio greater than 1.023, reducing the regime of interaction to one that is not highly correlated with ΔXCO_2. In the QF = 1 regime, h2o_ratio corresponds to a significant negative bias. Larger values of h2o_ratio are explained in Taylor et al. (2016), where it was shown that retrieved surface albedo from the strong CO_2 band is generally lower than the weak CO_2 band. In cases of larger aerosol presence, this sensitivity leads to weakening of the absorption features and a positive departure from unity. The additional albedo term for the strong CO_2 band and the additional aerosol terms also increase in importance for QF = 1.

For ocean QF = 1 data, there is a significant change in information gain for several features. The surface pressure delta term dp_sco2 becomes significantly less informative for correcting QF = 1, where negative values of dp_sco2 are relatively uncorrelated with ΔXCO_2. Similarly to land, the albedo term for the strong CO_2 band is more informative for correcting outside the filtered regime along with the residual error between forward-modeled radiances and measurements in the weak CO_2 band.

5.3 Preservation of CO_2 enhancements

We assess the risk of the proposed bias correction to correct and remove plume features in the data. Several features heavily utilized by the XGBoost models and in operational correction, such as the CO_2 gradient delta and surface pressure terms (e.g., dpfrac, dp_o2a), are differences between the ACOS-retrieved state and the prior. Therefore, there is potentially a risk for the bias correction to use the delta terms to overcorrect the retrieved XCO_2 to the truth. We compare XGBoost-corrected XCO_2 for two known plumes first identified in Nassar et al. (2021). The two example plumes are shown in Fig. 10a and b: an ocean glint and land nadir plume in Taean, South Korea, and a land nadir plume observed over two co-located power plants in Ohio, USA. We com-
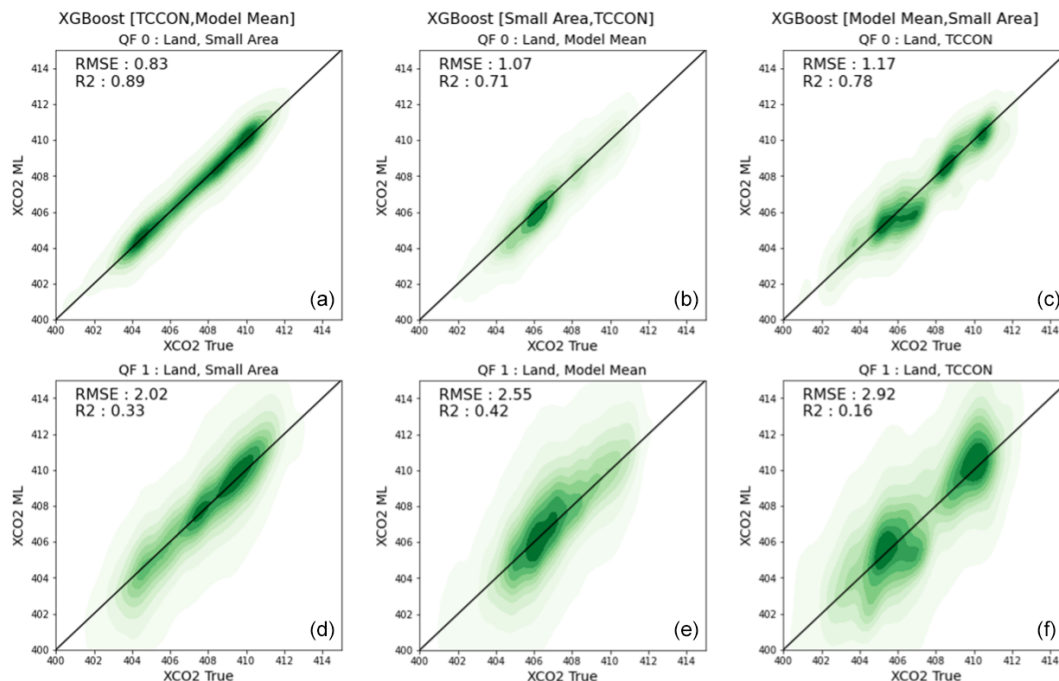
Figure 7. Comparison of XCO$_2$ derived from XCO$_2$ corrected by XGBoost (XCO$_2$ ML) vs. truth proxy (XCO$_2$ True) for land by the hold-out proxy set and hold-out year (2018). Panels **(a)** and **(d)** display results of a XGBoost model trained on [TCCON, Model Mean] and evaluated on Small Area. Panels **(b)** and **(e)** display results of a XGBoost model trained on [Small Area,TCCON] and evaluated on Model Mean. Panels **(c)** and **(f)** display results of a XGBoost model trained on [Model Mean, Small Area] and evaluated on TCCON. Generalization for the hold proxy and QF = 0 is shown in the top row and QF = 1 in the bottom.
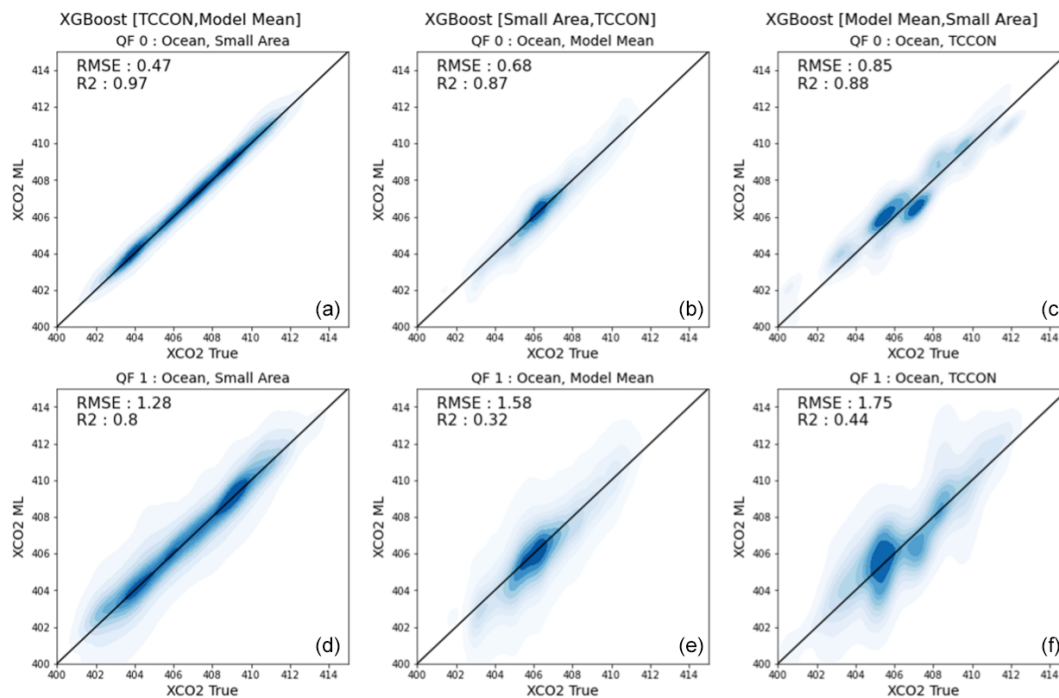

Figure 8. Comparison of XCO$_2$ derived from XCO$_2$ corrected by XGBoost (XCO$_2$ ML) vs. truth proxy (XCO$_2$ True) for ocean by the hold-out proxy set and hold-out year (2018). Panels **(a)** and **(d)** display results of a XGBoost model trained on [TCCON,Model Mean] and evaluated on Small Area. Panels **(b)** and **(e)** display results of a XGBoost model trained on [Small Area,TCCON] and evaluated on Model Mean. Panels **(c)** and **(f)** display results of a XGBoost model trained on [Model Mean, Small Area] and evaluated on TCCON. Generalization for the hold proxy and QF = 0 is shown in the top row and QF = 1 in the bottom.
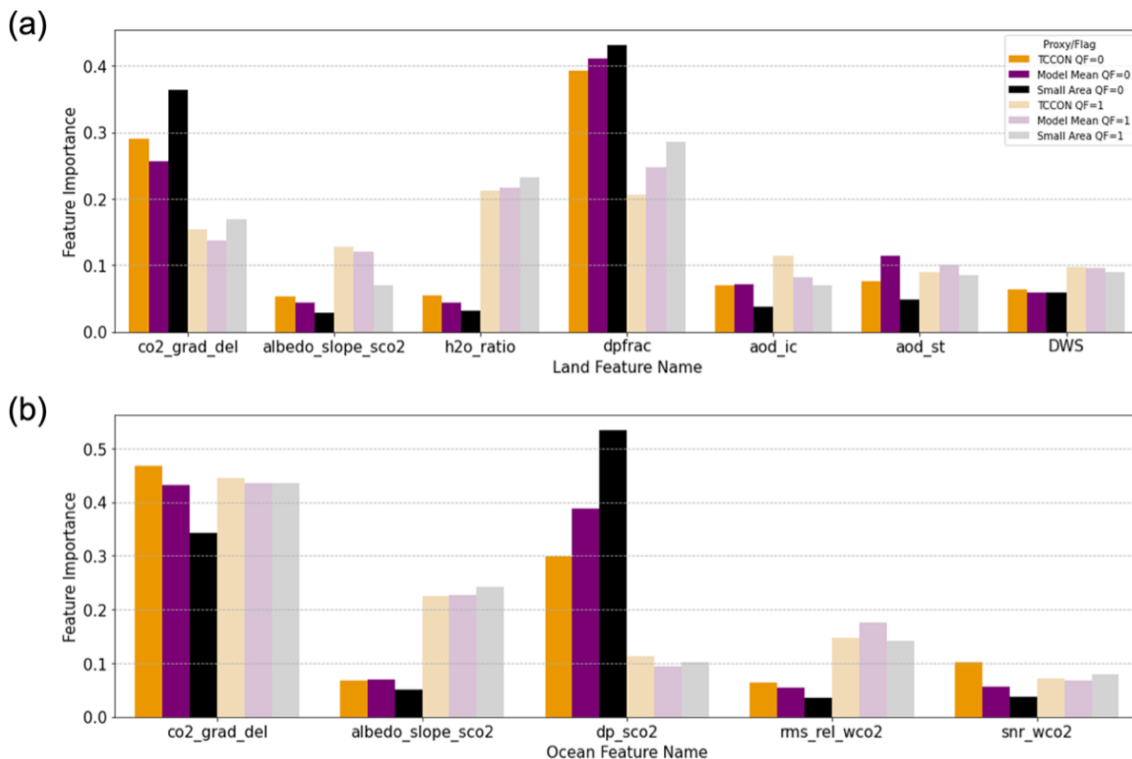
Figure 9. Feature importance for land is shown in panel **(a)**, and feature importance for ocean is shown in panel **(b)**. Y axis displays the normalized information gain from XGBoost models, with $QF = 0$ shown in darker colors and $QF = 1$ shown in lighter colors.

pare the uncorrected XCO$_2$ retrieval (B10 raw), the operationally corrected XCO$_2$ (B10 corrected), and the machine-learning-corrected XCO$_2$ (XGBoost corrected) and note that the machine-learning-corrected product captures enhancements not present in the training data. These results are also consistent with the findings in Mauceri et al. (2023), which include similar delta terms. This is further illustrated with the Taean plume which consists of $\sim 35\%$ QF = 0 soundings and ~ 65 QF = 1 soundings. QFNew = 0 improves the passing rate to $\sim 60\%$, as shown in Fig. 10c. The red stars show data that are passed by QF = 0 (and by construction QFNew = 0), and the blue stars show data that would be removed by QF = 1 but are passed by QFNew = 0, indicating where the increase in available data for the plume feature is. Of particular interest is the increase in data within the feature around 36.95°, which includes maximum observed enhancement value.

5.4 Potential for further improving data throughput

Figure 11 further illustrates how the shape of the filtering or decision surface can affect data throughput. Soundings are binned by two state vector features: h2o_ratio and dpfrac. Figure 11b and d show the improvement in the reduction of mean ∆XCO$_2$ and of the error divided by the posterior uncertainty from the nonlinear correction. The QF filters for each feature are indicated by the black dashed lines, and the

interior of the intersection of these filters indicates the region of state space that is labeled as QF = 0 (note: the additional filters of the QF further reduce the data that are passed in this region). Significant portions of the distribution, which the nonlinear method can accurately correct, lay outside of this filtered region and are labeled QF = 1. A data-driven filter can be constructed using similar interpretable machine learning techniques and produce a unified correction and filtering product. Furthermore, moving away from the binary quality flag to a ternary ("very good", "good", "bad") will likely provide an improved data product for end users. Data-driven methods for quality filtering have already proven to be useful in the northern high latitudes (Mendonca et al., 2021), and a genetic algorithm was previously used to derive the "warn levels" which complement the operational quality flag found in early OCO-2 data versions (Mandrake et al., 2015). An important task for such future work will be to ensure that the machine learning method learns a physically consistent filter that can increase data throughput while still limiting variance of error and ∆XCO$_2$. We also acknowledge that while the Taean plume shown in Fig. 10 illustrates an empirical example of the ability of a nonlinear correction to improve throughput of good-quality data, further evaluation of the intersection (QF = 1 and QFNew = 0) will be required before bringing such a method to operation.
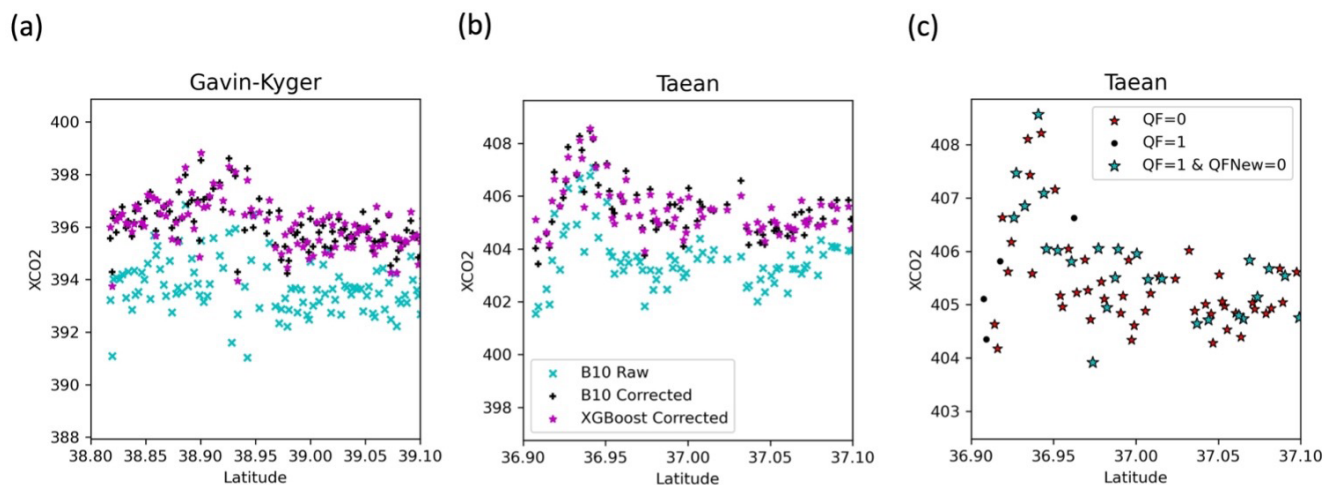
Figure 10. Two CO$_2$ plumes captured downwind from power plants (Nassar et al., 2021). A land nadir plume near the J. M. Gavin and Kyger Creek power plants in Ohio, USA (lat 38.93°, long −82.12°), on 30 July 2015 **(a)**. An ocean glint and land nadir plume at Taean, South Korea (lat 36.91°, long 126.23°), on 17 April 2015 are shown in panel **(b)**. Regions with the example plumes are not present in the training dataset and consist of QF = 0 + 1 data. Panel **(c)** shows the increase in XGBoost-corrected data for QFNew = 0 that would be filtered by the B10 QF.
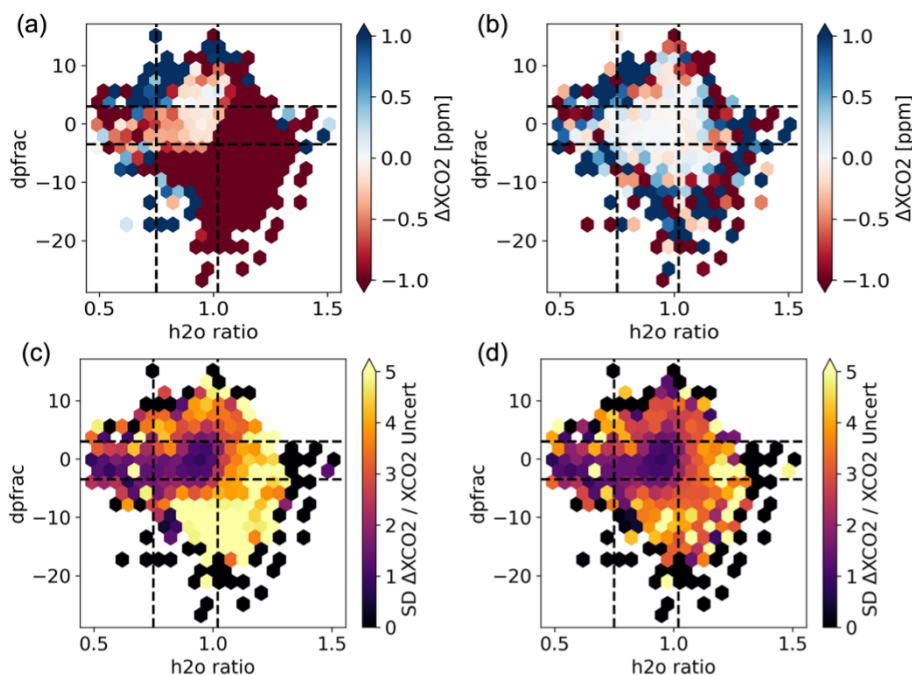
Figure 11. Hex bin plots show conditional distributions of 2018 ΔXCO$_2$ vs. dpfrac and h2o_ratio. Remaining ΔXCO$_2$ after the operational correction for B10 is shown in panel **(a)**. Remaining ΔXCO$_2$ after the nonlinear correction is shown in panel **(b)**. Binned SD of ΔXCO$_2$ divided by the posterior uncertainty from the retrieved X$_{CO_2}$ is shown in panel **(c)** for the operational correction for B10 and panel **(d)** for the nonlinear correction. B10 QF filter thresholds for both features are shown with black dashed lines for reference.

6 Conclusion

We demonstrate an approach for selecting co-retrieved state vector variables and other features to be used as input for a land model and an ocean model to correct biases in ACOS-retrieved XCO$_2$. The use of the nonlinear method allows for decoupling of the dependent bias correction and filter used in operation, as the filter no longer needs to limit the correction function to a linear fit. By doing so, this method achieves a 59 % and 67 % improvement in the reduction of the error variance over the operational correction on QF = 1 data for

land and ocean, respectively. To utilize this improvement in correction, we derive a new quality flag (QFNew) by relaxing select filter thresholds from the operational quality flag. Using the proposed QFNew flag, we increase data throughput by 14 % while maintaining a comparable residual error to the operational B10 correction. The workflow outlined in this research is extendable to future ACOS algorithm updates and OCO-2's companion instrument, OCO-3, on board the International Space Station.

Appendix A: Feature selection and importance

To assess the robustness of our choice of features, we compare the ranking produced by the information gain feature importance generated by the gradient booster with the ranking produced by a method called permutation feature importance (Fisher et al., 2018). Permutation feature importance captures the contribution to residual error when a feature has its values randomly shifted across observations. Permutation feature importance is a model-agnostic post hoc method that does not require the bias correction model to be retrained. In Fig. A1 we compare the normalized rankings for the individual proxy/surface/mode models that were used to select variables for the final bias correction models trained on all truth proxies. Good agreement is observed in both the overall ranking and magnitude of normalized feature importance between both methods.

The feature importance from the models trained on individual proxies and QF = 0 + 1 data was used to identify state variables to be used as input for the proposed bias correction models. While there is generally good agreement between the proxies, the overall magnitude and ranking differ slightly, as shown in Fig. A2. For TCCON the aerosols and albedo terms contribute more to the correction, while the same terms are less informative for the small area approximation, which is likely due to the small area proxy capturing biases that vary slowly over larger scales. For ocean, the albedo_slope_sco2 is informative for the small area proxy, and all proxies exhibit better agreement in their feature importance.
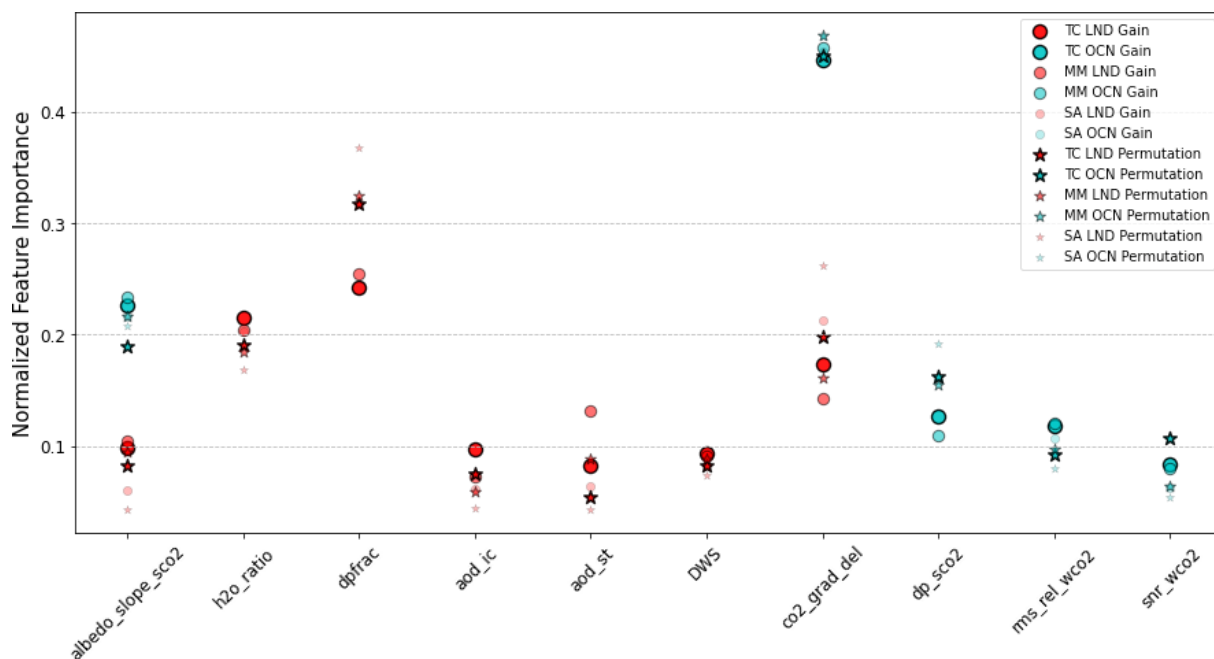
Figure A1. Comparison of feature importance derived from information gain and permutation importance. Normalized importance (permutation importance in stars and information gain in circles) is shown for land and ocean features and by truth proxy. The feature importance produced by both methods is largely in agreement in ranking and overall contribution.
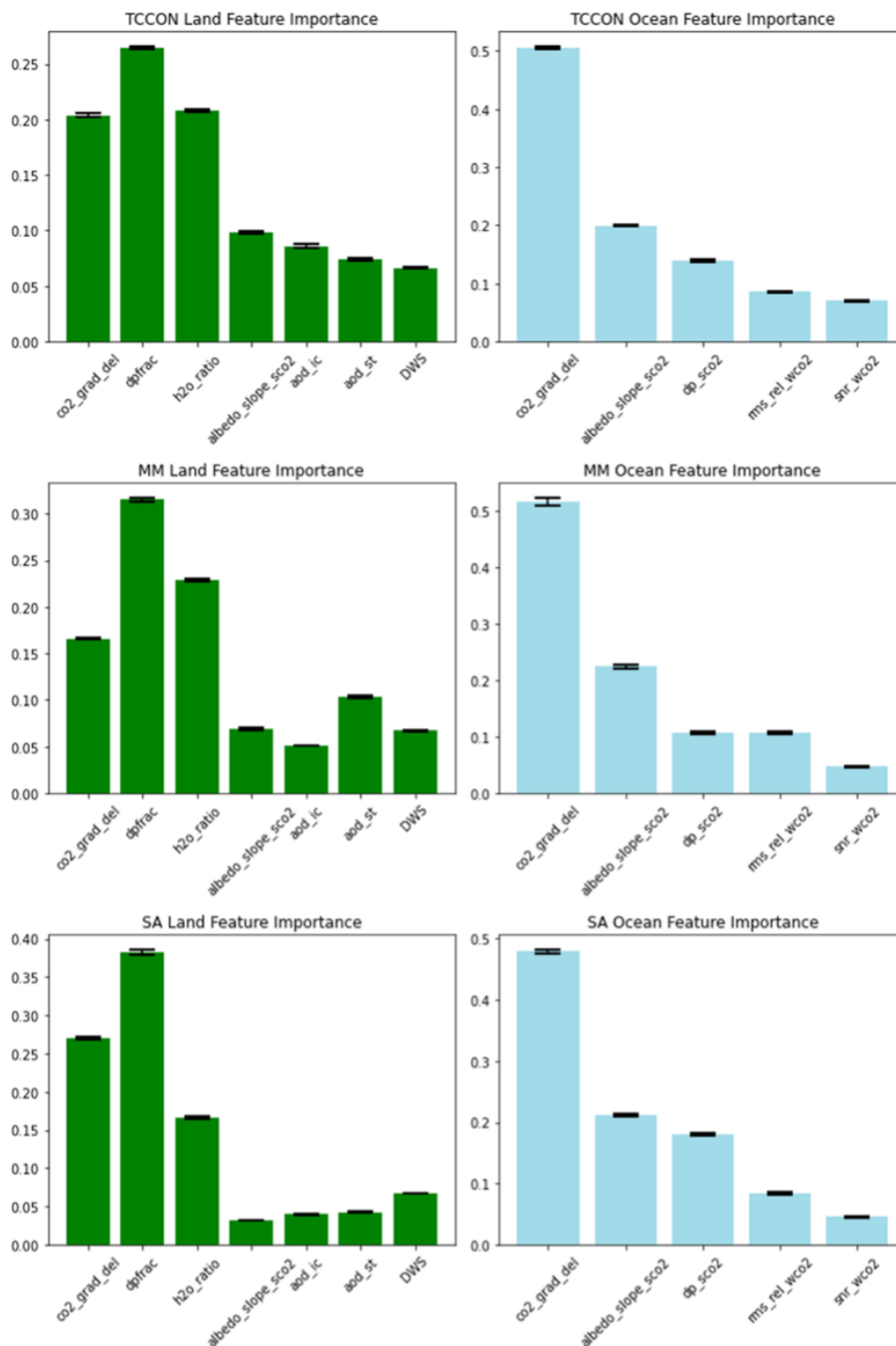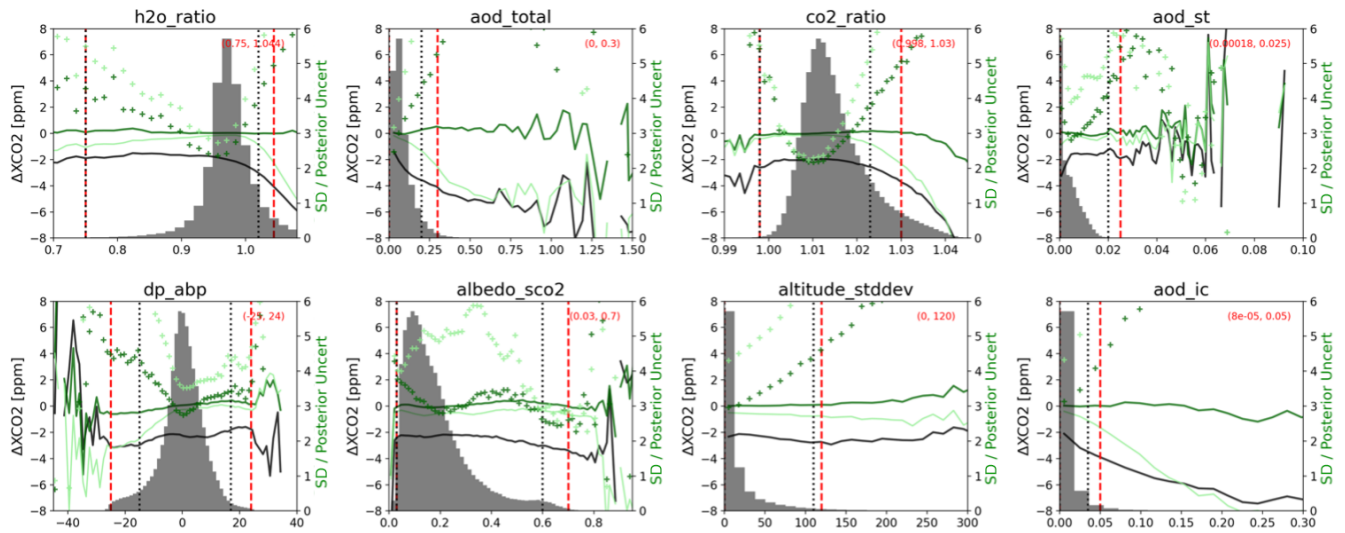
Figure A2. Feature importance for individual truth proxy models. Error bars indicate variance over 10 runs with different random seeds.

Appendix B: Threshold values for QFNew

Figure B1. Variables selected for land QFNew: the difference between the uncorrected retrieval and the model mean truth proxy is shown with the black curve. The difference between the operational correction and the model mean truth proxy is shown in the light green curve. The difference after the nonlinear correction is shown by the dark green curve. The binned SD error divided by the posterior uncertainty of XCO$_2$ is shown by the green pluses and right y axis. B10 QF filters are indicated by the vertical black dashed lines, and QFNew is shown by the red dashed lines. Region of data denoted as QFNew $= 0$ is contained within the red values in the parentheses.
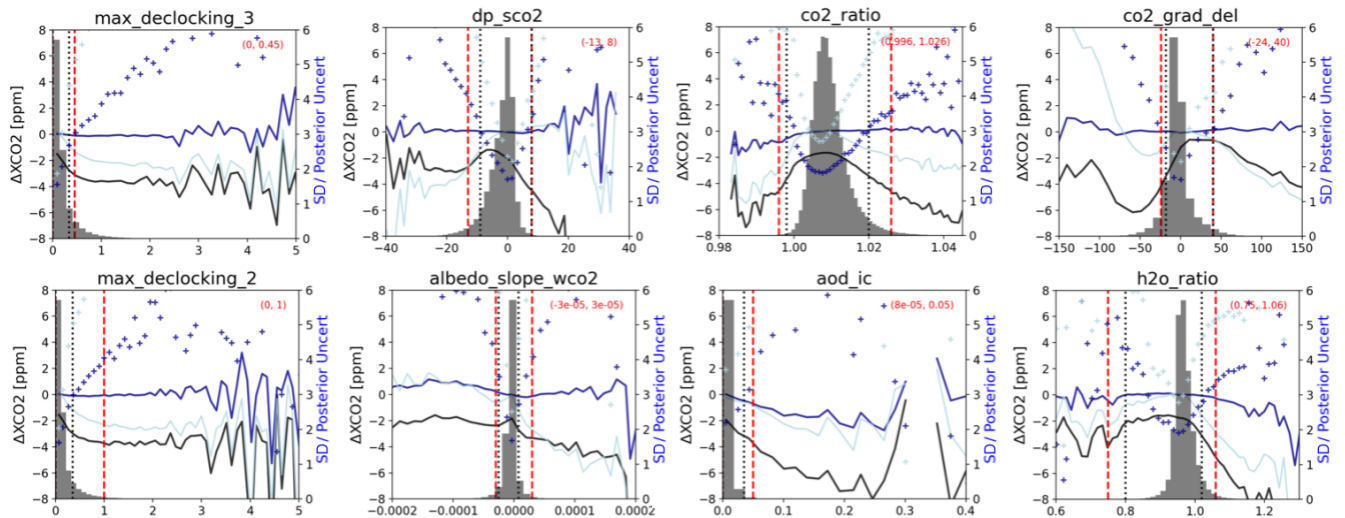
Figure B2. Variables selected for ocean QFNew: the difference between the raw uncorrected retrieval and the model mean truth proxy is shown with the black curve. The difference between the operational correction and the model mean truth proxy is shown by the light blue curve. The difference after the nonlinear correction is shown by the dark blue curve. The binned SD error divided by the posterior uncertainty of XCO$_2$ is shown by the blue pluses and right y axis. B10 filters are indicated by the vertical black dashed lines, and a potential filter is shown by the red dashed lines. Region of data denoted as QFNew $= 0$ is contained within the red values in the parentheses.

Appendix C: Lite file variables

Table C1. Features used or considered for the operational and proposed bias correction and filtering. BC stands for B10 bias correction, and ML BC stands for XGBoost bias correction.

State variable	Description	Used for B10 BC, ML BC, QF, QFNew
dpfrac	Surface pressure difference that considers smaller dry air columns over higher elevations (Kiel et al., 2019).	B10 BC, ML BC, QF, QFNew
h2o_ratio	Ratio of retrieved H_2O column in weak and strong CO_2 bands by IMAP-DOAS.	ML BC, QF, QFNew*
DWS	Additive combination of retrieved dust, water, and sea salt aerosol optical depth.	B10 BC, ML BC, QF, QFNew
aod_strataer	Retrieved upper-tropospheric plus stratospheric aerosol optical depth at 0.755 μm.	ML BC, QF, QFNew
aod_ice	Retrieved ice cloud optical depth at 0.755 μm.	ML BC, QF, QFNew*
co2_grad_del	Difference between the retrieved vertical CO_2 profile and prior.	B10 BC, ML BC, QF, QFNew
dp_sco2	Surface pressure difference between the retrieved and prior, evaluated for the strong CO_2 band location on the ground.	B10 BC, ML BC, QF, QFNew*
snr_wco2	The estimated signal-to-noise ratio in the continuum of the weak CO_2 band.	ML BC, QF, QFNew
co2_ratio	Ratio of retrieved CO_2 column in the weak and strong CO_2 bands by IMAP-DOAS.	QF, QFNew*
altitude_stddev	The standard deviation of the surface elevation in the target field of view. Unit is in meters.	QF, QFNew*
max_declocking_wco2	An estimate of the absolute value of the clocking error in the weak CO_2 band, expressed as a percent.	QF, QFNew*
max_declocking_sco2	An estimate of the absolute value of the clocking error in the strong CO_2 band, expressed as a percent.	QF, QFNew*
dp_o2a	The difference in retrieved surface pressure to O_2 A band surface pressure prior.	QF, QFNew
dp_abp	The difference in the retrieved surface pressure to the fast O_2 A band preprocessor retrieval.	QF, QFNew*
albedo_slope_sco2	Retrieved strong band reflectance slope (land) or slope of Lambertian albedo component of BRDF (ocean).	ML BC, QF, QFNew
albedo_slope_wco2	Slope of the weak CO_2 band albedo with respect to wavenumber.	QF, QFNew*
albedo_sco2	Surface reflectance at a reference wavelength in the strong CO_2 band in the primary scattering geometry from the retrieved BRDF (land) and retrieved Lambertian albedo (ocean).	QF, QFNew*
albedo_quad_sco2	Quadratic coefficient of the albedo_sco2 term with respect to wavenumber (land only).	QF, QFNew
albedo_quad_wco2	Quadratic coefficient of the albedo_wco2 term with respect to wavenumber (land only).	QF, QFNew
aod_total	Retrieved aerosol optical depth of cloud and aerosol at 0.755 μm.	QF, QFNew*
rms_rel_sco2	RMSE of the L2 fit residuals in the strong CO_2 band relative to the signal.	QF, QFNew
rms_rel_wco2	RMSE of the L2 fit residuals in the weak CO_2 band relative to the signal.	ML BC, QF, QFNew
detlaT	Retrieved offset to prior temperature profile in Kelvin.	QF, QFNew
aod_sulfate	Retrieved aerosol optical depth of sulfate aerosol at 0.755 μm.	B10 BC, QF, QFNew
aod_oc	Retrieved aerosol optical depth of organic carbon aerosol at 0.755 μm.	B10 BC, QF, QFNew
aod_water	Retrieved aerosol optical depth of water aerosol at 0.755 μm.	QF, QFNew
dust_height	Retrieved central pressure of the dust aerosol layer, relative to the retrieved surface pressure.	QF, QFNew
aod_seasalt	Retrieved aerosol optical depth of sea salt aerosol at 0.755 μm.	QF, QFNew
Fs_rel	Retrieved fluorescence relative to the O_2A band continuum signal.	QF, QFNew
chi2_wco2	Reduced chi-squared value of the L2 fit residuals for the weak CO_2 band.	QF, QFNew
windspeed	Retrieved surface wind speed over water surfaces.	QF, QFNew
water_height	Retrieved central pressure of the cloud water layer, relative to the retrieved surface pressure.	QF, QFNew

* Changed filter threshold for QFNew.

References

Aumann, H. H., Chahine, M. T., Gautier, C., Goldberg, M. D., Kalnay, E., McMillin, L. M., Revercomb, H., Rosenkranz, P. W., Smith, W. L., Staelin, D. H., Strow, L. L., and Susskind, J.: AIRS/AMSU/HSB on the Aqua mission: Design, science objectives, data products, and processing systems, IEEE T. Geosci. Remote, 41, 253–264, https://doi.org/10.1109/tgrs.2002.808356, 2003.

Blumenstock, T., Hase, F., Schneider, M., Garcia, O. E., and Sepulveda, E.: TCCON data from Iza na (ES), Release GGG2014R1, TCCON data archive, CaltechDATA [data set], https://doi.org/10.14291/TCCON.GGG2014.IZANA01.R1, 2017.

Bovensmann, H., Burrows, J. P., Buchwitz, M., Frerick, J., Nöel, S., Rozanov, V. V., Chance, K. V., and Goede, A.: SCIAMACHY—Mission objectives and measurement modes, J. Atmos. Sci., 56, 127–150, https://doi.org/10.1175/1520-0469(1999)056<0127:SMOAMM>2.0.CO;2, 1999.

Breiman, L.: Classification and Regression Trees, 1st edn., Routledge, New York, https://doi.org/10.1201/9781315139470, 1984.

CAMS (Copernicus Atmosphere Monitoring Service): Validation report for the CO_2 fluxes estimated by atmospheric inversion, v18r2, Version 1.0, https://atmosphere.copernicus.eu/sites/default/files/2019-08/CAMS73_2018SC1_D73.1.4.1-2018-v1_201907_v1.pdf (last access: 10 January 2022), 2021.

CarbonTracker: CarbonTracker, NOAA ESRL, https://carbontracker.noaa.gov (last access: 10 January 2022), 2021.

CarboScope: CarboScope, Max Planck Institute for Biogeochemistry, Jena, https://www.bgc-jena.mpg.de/CarboScope (last access: 10 January 2022), 2021.

Chen, T. and Guestrin, C.: XGBoost: A Scalable Tree Boosting System, in: Proceedings of the 22nd ACM SIGKDD International Conference on Knowledge Discovery and Data Mining – KDD"16, ACM Press, New York, New York, USA, 785–794, 2016.

Chevallier, F., Ciais, P., Conway, T. J., Aalto, T., Anderson, B. E., Bousquet, P., Brunke, E. G., Ciattaglia, L., Esaki, Y., Fröhlich, M., Gomez, A., Gomez-Pelaez, A. J., Haszpra, L., Krummel, P. B., Langenfelds, R. L., Leuenberger, M., Machida, T., Maignan, F., Matsueda, H., Morguí, J. A., Mukai, H., Nakazawa, T., Peylin, P., Ramonet, M., Rivier, L., Sawa, Y., Schmidt, M., Steele, L. P., Vay, S. A., Vermeulen, A. T., Wofsy, S., and Worthy, D.: CO_2 surface fluxes at grid point scale estimated from a global 21 year reanalysis of atmospheric measurements, J. Geophys. Res., 115, D21307, https://doi.org/10.1029/2010JD013887, 2010.

Connor, B. J., Bösch, H., Toon, G., Sen, B., Miller, C., and Crisp, D.: Orbiting Carbon Observatory: Inverse method and prospective error analysis, J. Geophys. Res., 113, A05305, https://doi.org/10.1029/2006JD008336, 2008.

Cox, C. and Munk, W. H.: The measurement of the roughness of the sea surface from photographs of the sun's glitter, J. Opt. Soc. Am., 44, 838–850, 1954.

Crisp, D., Atlas, R. M., Breon, F. M., Brown, L. R., Burrows, J. P., Ciais, P., Connor, B. J., Doney, S. C., Fung, I. Y., Jacob, D. J., Miller, C. E., O'Brien, D., Pawson, S., Randerson, J. T., Rayner, P., Salawitch, R. J., Sander, S. P., Sen, B., Stephens, G. L., Tans, P. P., Toon, G. C., Wennberg, P. O., Wofsy, S. C., Yung, Y. L., Kuang, Z., Chudasama, B., Sprague, G., Weiss, B., Pollock, R., Kenyon, D., and Schroll, S.: The Orbiting Carbon Observatory (OCO) mission, Adv. Space Res., 34, 700–709, https://doi.org/10.1016/j.asr.2003.08.062, 2004.

Crisp, D., Fisher, B. M., O'Dell, C., Frankenberg, C., Basilio, R., Bösch, H., Brown, L. R., Castano, R., Connor, B., Deutscher, N. M., Eldering, A., Griffith, D., Gunson, M., Kuze, A., Mandrake, L., McDuffie, J., Messerschmidt, J., Miller, C. E., Morino, I., Natraj, V., Notholt, J., O'Brien, D. M., Oyafuso, F., Polonsky, I., Robinson, J., Salawitch, R., Sherlock, V., Smyth, M., Suto, H., Taylor, T. E., Thompson, D. R., Wennberg, P. O., Wunch, D., and Yung, Y. L.: The ACOS CO_2 retrieval algorithm – Part II: Global X_{CO_2} data characterization, Atmos. Meas. Tech., 5, 687–707, https://doi.org/10.5194/amt-5-687-2012, 2012.

Crisp, D., Pollock, H. R., Rosenberg, R., Chapsky, L., Lee, R. A. M., Oyafuso, F. A., Frankenberg, C., O'Dell, C. W., Bruegge, C. J., Doran, G. B., Eldering, A., Fisher, B. M., Fu, D., Gunson, M. R., Mandrake, L., Osterman, G. B., Schwandner, F. M., Sun, K., Taylor, T. E., Wennberg, P. O., and Wunch, D.: The on-orbit performance of the Orbiting Carbon Observatory-2 (OCO-2) instrument and its radiometrically calibrated products, Atmos. Meas. Tech., 10, 59–81, https://doi.org/10.5194/amt-10-59-2017, 2017.

Crowell, S., Baker, D., Schuh, A., Basu, S., Jacobson, A. R., Chevallier, F., Liu, J., Deng, F., Feng, L., McKain, K., Chatterjee, A., Miller, J. B., Stephens, B. B., Eldering, A., Crisp, D., Schimel, D., Nassar, R., O'Dell, C. W., Oda, T., Sweeney, C., Palmer, P. I., and Jones, D. B. A.: The 2015–2016 carbon cycle as seen from OCO-2 and the global in situ network, Atmos. Chem. Phys., 19, 9797–9831, https://doi.org/10.5194/acp-19-9797-2019, 2019.

De Mazière, M., Sha, M. K., Desmet, F., Hermans, C., Scolas, F., Kumps, N., Metzger, J.-M., Duflot, V., and Cammas, J.-P.: TCCONdata from Réunion Island (RE), Release GGG2014.R1, TCCON data archive, CaltechDATA [data set], https://doi.org/10.14291/TCCON.GGG2014.REUNION01.R1, 2017.

Deutscher, N. M., Notholt, J., Messerschmidt, J., Weinzierl, C., Warneke, T., Petri, C., and Grupe, P.: TCCON data from Bialystok (PL), Release GGG2014.R2, TCCON data archive, CaltechDATA [data set], https://doi.org/10.14291/TCCON.GGG2014.BIALYSTOK01.R2, 2019.

Dubey, M. K., Lindenmaier, R., Henderson, B. G., Green, D., Allen, N. T., Roehl, C. M., Blavier, J.-F., Butterfield, Z. T., Love, S., Hamelmann, J. D., and Wunch, D.: TCCON data from Four Corners (US), Release GGG2014.R0, TCCON data archive, CaltechDATA [data set], https://doi.org/10.14291/TCCON.GGG2014.FOURCORNERS01.R0/1149272, 2014.

Fisher, A., Cynthia R., and Francesca D.: All models are wrong, but many are useful: Learning a variable's importance by studying an entire class of prediction models simultaneously, arXiv [preprint], https://doi.org/10.48550/arXiv.1801.01489, 23 December 2018.

Frankenberg, C., Platt, U., and Wagner, T.: Iterative maximum a posteriori (IMAP)-DOAS for retrieval of strongly absorbing trace gases: Model studies for CH$_4$ and CO$_2$ retrieval from near infrared spectra of SCIAMACHY onboard ENVISAT, Atmos. Chem. Phys., 5, 9–22, https://doi.org/10.5194/acp-5-9-2005, 2005.

Goo, T.-Y., Oh, Y.-S., and Velazco, V. A.: TCCON data from Anmeyondo (KR), Release GGG2014.R0, TCCON data archive, CaltechDATA [data set], https://doi.org/10.14291/TCCON.GGG2014.ANMEYONDO01.R0/1149284, 2014.

Griffith, D. W., Deutscher, N. M., Velazco, V. A., Wennberg, P. O., Yavin, Y., Aleks, G. K., Washenfelder, R. A., Toon, G. C., Blavier, J.-F., Murphy, C., Jones, N., Kettlewell, G., Connor, B. J., Macatangay, R., Roehl, C., Ryczek, M., Glowacki, J., Culgan, T., and Bryant, G.: TCCONdatafromDarwin(AU), Release GGG2014R0, TCCON data archive, CaltechDATA [data set], https://doi.org/10.14291/tccon.ggg2014.darwin01.R0/1149290, 2014a.

Griffith, D. W., Velazco, V. A., Deutscher, N. M., Murphy, C., Jones, N., Wilson, S., Macatangay, R., Kettlewell, G., Buchholz, R. R., and Riggenbach, M.: TCCON data from Wollongong (AU), Release GGG2014R0, TCCON data archive, CaltechDATA [data set], https://doi.org/10.14291/tccon.ggg2014.wollongong01.R0/1149291, 2014b.

Hase, F., Blumenstock, T., Dohe, S., Gross, J., and Kiel, M.: TCCON data from Karlsruhe (DE), Release GGG2014R1, TCCON data archive, CaltechDATA [data set], https://doi.org/10.14291/tccon.ggg2014.karlsruhe01.R1/1182416, 2015.

Jacobs, N., Simpson, W. R., Wunch, D., O'Dell, C. W., Osterman, G. B., Hase, F., Blumenstock, T., Tu, Q., Frey, M., Dubey, M. K., Parker, H. A., Kivi, R., and Heikkinen, P.: Quality controls, bias, and seasonality of CO$_2$ columns in the boreal forest with Orbiting Carbon Observatory-2, Total Carbon Column Observing Network, and EM27/SUN measurements, Atmos. Meas. Tech., 13, 5033–5063, https://doi.org/10.5194/amt-13-5033-2020, 2020.

Keely, W. R.: AMT ML bias correction OCO-2, OSF [data set], https://doi.org/10.17605/OSF.IO/CX53S, 2023.

Kiel, M., O'Dell, C. W., Fisher, B., Eldering, A., Nassar, R., MacDonald, C. G., and Wennberg, P. O.: How bias correction goes wrong: measurement of XCO$_2$ affected by erroneous surface pressure estimates, Atmos. Meas. Tech., 12, 2241–2259, https://doi.org/10.5194/amt-12-2241-2019, 2019.

Kivi, R., Heikkinen, P., and Kyrö, E.: TCCON from Sodankylä (FI), Release GGG2014.R0, TCCON data archive, CaltechDATA [data set], https://doi.org/10.14291/tccon.ggg2014.sodankyla01.R0/1149280, 2014.

Kulawik, S. S., O'Dell, C., Nelson, R. R., and Taylor, T. E.: Validation of OCO-2 error analysis using simulated retrievals, Atmos. Meas. Tech., 12, 5317–5334, https://doi.org/10.5194/amt-12-5317-2019, 2019.

Kuze, A., Suto, H., Nakajima, M., and Hamazaki, T.: Initial Onboard Performance of TANSO-FTS on GOSAT, in: Advances in Imaging, OSA Technical Digest (CD), (Optica Publishing Group, 2009), https://doi.org/10.1364/FTS.2009.FTuC2, 2009.

Liu, J., Bowman, K. W., Schimel, D. S., Parazoo, N. C., Jiang, Z., Lee, M., Bloom, A. A., Wunch, D., Frankenberg, C., Sun, Y., O'Dell, C. W., Gurney, K. R., Menemenlis, D., Gierach, M., Crisp, D., and Eldering, A.: Contrasting carbon cycle responses of the tropical continents to the 2015–2016 El Niño, Science, 358, eaam5690, https://doi.org/10.1126/science.aam5690, 2017.

Mandrake, L., O'Dell, C. W., Wunch, D., Wennberg, P. O., Fisher, B., Osterman, G. B., and Eldering, A.: Orbiting Carbon Observatory-2 (OCO-2) Warn Level, Bias Correction, and Lite File Product Description, Tech. rep., Jet Propulsion Laboratory, California Institute of Technology, Pasasdena, https://disc.sci.gsfc.nasa.gov/OCO-2/documentation/oco-2-v7/OCO2_XCO2_Lite_Files_and_Bias_Correction_0915_sm.pdf (last access: 16 October 2015), 2015.

Morino, I., Matsuzaki, T., and Horikawa, M.: TCCON data from Tsukuba (JP), 125HR, Release GGG2014R2, TCCON data archive, CaltechDATA [data set], https://doi.org/10.14291/TCCON.GGG2014.TSUKUBA02.R2, 2018a.

Morino, I., Velazco, V. A., Hori, A., Uchino, O., and Griffith, D. W. T.: TCCON data from Burgos, Ilocos Norte (PH), Release GGG2014.R0, TCCON data archive, CaltechDATA [data set], https://doi.org/10.14291/TCCON.GGG2014.BURGOS01.R0, 2018b.

Masarie, K. A., Peters, W., Jacobson, A. R., and Tans, P. P.: ObsPack: a framework for the preparation, delivery, and attribution of atmospheric greenhouse gas measurements, Earth Syst. Sci. Data, 6, 375–384, https://doi.org/10.5194/essd-6-375-2014, 2014.

Massie, S. T., Schmidt, S. K., Eldering, A., and Crisp, D.: Observational evidence of 3-D cloud effects in OCO-2 CO$_2$ retrievals, J. Geophys. Res., 122, 7064–7085, https://doi.org/10.1002/2016JD026111, 2016.

Mauceri, S., Massie, S., and Schmidt, S.: Correcting 3D cloud effects in X$_{CO_2}$ retrievals from the Orbiting Carbon Observatory-2 (OCO-2), Atmos. Meas. Tech., 16, 1461–1476, https://doi.org/10.5194/amt-16-1461-2023, 2023.

Mendonca, J., Nassar, R., O'Dell, C. W., Kivi, R., Morino, I., Notholt, J., Petri, C., Strong, K., and Wunch, D.: Assessing the feasibility of using a neural network to filter Orbiting Carbon Observatory 2 (OCO-2) retrievals at northern high latitudes, Atmos. Meas. Tech., 14, 7511–7524, https://doi.org/10.5194/amt-14-7511-2021, 2021.

Morino, I., Matsuzaki, T., and Horikawa, M.: TCCON data from Tsukuba (JP), 125HR, Release GGG2014R2, TCCON data archive, CaltechDATA [data set], https://doi.org/10.14291/TCCON.GGG2014.TSUKUBA02.R2, 2018a.

Morino, I., Velazco, V. A., Hori, A., Uchino, O., and Griffith, D. W. T.: TCCON data from Burgos, Ilocos Norte (PH), Release GGG2014.R0, TCCON data archive, CaltechDATA [data set], https://doi.org/10.14291/TCCON.GGG2014.BURGOS01.R0, 2018b.

Morino, I., Yokozeki, N., Matzuzaki, A., and Shishime, A.: TCCON data from Rikubetsu, Hokkaido, Japan, Release GGG2014R2, TCCON data archive, CaltechDATA [data set], https://doi.org/10.14291/TCCON.GGG2014.RIKUBETSU01.R2, 2018c.

Nassar, R., Hill, T. G., McLinden, C. A., Wunch, D., Jones, D. B. A., and Crisp, D.: Quantifying CO$_2$ Emissions From Individual Power Plants From Space, Geophys. Res. Lett., 44, 10045–10053, https://doi.org/10.1002/2017GL074702, 2017.

Nassar, R., Mastrogiacomo, J.-P., Bateman-Hemphill, W., McCracken, C., MacDonald, C. G., Hill, T., O'Dell, C. W., Kiel, M., and Crisp, D.: Advances in quantifying power plant CO$_2$ emissions with OCO-2, Remote Sens. Environ., 264, 112579, https://doi.org/10.1016/j.rse.2021.112579, 2021.

Noël, S., Reuter, M., Buchwitz, M., Borchardt, J., Hilker, M., Schneising, O., Bovensmann, H., Burrows, J. P., Di Noia, A., Parker, R. J., Suto, H., Yoshida, Y., Buschmann, M., Deutscher, N. M., Feist, D. G., Griffith, D. W. T., Hase, F., Kivi, R., Liu, C., Morino, I., Notholt, J., Oh, Y.-S., Ohyama, H., Petri, C., Pollard, D. F., Rettinger, M., Roehl, C., Rousogenous, C., Sha, M. K., Shiomi, K., Strong, K., Sussmann, R., Té, Y., Velazco, V. A., Vrekoussis, M., and Warneke, T.: Retrieval of greenhouse gases from GOSAT and GOSAT-2 using the FOCAL algorithm, Atmos. Meas. Tech., 15, 3401–3437, https://doi.org/10.5194/amt-15-3401-2022, 2022.

Notholt, J., Petri, C., Warneke, T., Deutscher, N. M., Palm, M., Buschmann, M., Weinzierl, C., Macatangay, R. C., and Grupe, P.: TCCON data from Bremen (DE), Release GGG2014.R1, TCCON data archive, CaltechDATA [data set], https://doi.org/10.14291/TCCON.GGG2014.BREMEN01.R1, 2019.

O'Dell, C. W., Connor, B., Bösch, H., O'Brien, D., Frankenberg, C., Castano, R., Christi, M., Eldering, D., Fisher, B., Gunson, M., McDuffie, J., Miller, C. E., Natraj, V., Oyafuso, F., Polonsky, I., Smyth, M., Taylor, T., Toon, G. C., Wennberg, P. O., and Wunch, D.: The ACOS CO$_2$ retrieval algorithm – Part 1: Description and validation against synthetic observations, Atmos. Meas. Tech., 5, 99–121, https://doi.org/10.5194/amt-5-99-2012, 2012.

O'Dell, C. W., Eldering, A., Wennberg, P. O., Crisp, D., Gunson, M. R., Fisher, B., Frankenberg, C., Kiel, M., Lindqvist, H., Mandrake, L., Merrelli, A., Natraj, V., Nelson, R. R., Osterman, G. B., Payne, V. H., Taylor, T. E., Wunch, D., Drouin, B. J., Oyafuso, F., Chang, A., McDuffie, J., Smyth, M., Baker, D. F., Basu, S., Chevallier, F., Crowell, S. M. R., Feng, L., Palmer, P. I., Dubey, M., García, O. E., Griffith, D. W. T., Hase, F., Iraci, L. T., Kivi, R., Morino, I., Notholt, J., Ohyama, H., Petri, C., Roehl, C. M., Sha, M. K., Strong, K., Sussmann, R., Te, Y., Uchino, O., and Velazco, V. A.: Improved retrievals of carbon dioxide from Orbiting Carbon Observatory-2 with the version 8 ACOS algorithm, Atmos. Meas. Tech., 11, 6539–6576, https://doi.org/10.5194/amt-11-6539-2018, 2018.

OCO-2 Science Team, Gunson, M., and Eldering, A.: OCO-2 Level 2 bias-corrected XCO$_2$ and other select fields from the full-physics retrieval aggregated as daily files, Retrospective processing V10r, Goddard Earth Sciences Data and Information Services Center (GES DISC) [data set], Greenbelt, MD, USA, https://doi.org/10.5067/E4E140XDMPO2, 2020.

Osterman, G. B., O'Dell, C. W., Eldering, A., Fisher, B., Crisp, D., Cheng, C., Frankenberg, C., Lambert, A., Gunson, M. R., Mandrake, L., and Wunch, D.: Orbiting Carbon Observatory-2 & 3 (OCO-2 & OCO-3) Data Product User's Guide, Operational Level 2 Data Versions 10 and Lite File Version 10 and VEarly, National Aeronautics and Space Administration Jet Propulsion Laboratory California Institute of Technology Pasadena, California, https://docserver.gesdisc.eosdis.nasa.gov/public/project/OCO/OCO2_OCO3_B10_DUG.pdf (last access: 22 July 2023), 2020.

Palmer, P. I., Feng, L., Baker, D., Chevallier, F., Hartman, B., and Somkuti P.: Net carbon emissions from African biosphere dominate pan-tropical atmospheric CO$_2$ signal, Nat. Commun., 10, 3344, https://doi.org/10.1038/s41467-019-11097-w, 2019.

Payne, V., Chatterjee, A., Rosenberg, R., Kiel, M., Fisher, B., Dang, L., O'Dell, C., Taylor, T., and Osterman, G.: Orbiting Carbon Observatory-2 & 3 Data Product User's Guide, OCO-2 v11 and OCO-3 v10.4, Tech. rep., Jet Propulsion Laboratory, https://docserver.gesdisc.eosdis.nasa.gov/public/project/OCO/OCO2_V11_OCO3_V10_DUG.pdf (last access: 2 July 2023), 2022.

Peiro, H., Crowell, S., Schuh, A., Baker, D. F., O'Dell, C., Jacobson, A. R., Chevallier, F., Liu, J., Eldering, A., Crisp, D., Deng, F., Weir, B., Basu, S., Johnson, M. S., Philip, S., and Baker, I.: Four years of global carbon cycle observed from the Orbiting Carbon Observatory 2 (OCO-2) version 9 and in situ data and compar-

ison to OCO-2 version 7, Atmos. Chem. Phys., 22, 1097–1130, https://doi.org/10.5194/acp-22-1097-2022, 2022.

Peters, W., Jacobson, A. R., Sweeney, C., Andrews, A. E., Conway, T. J., Masarie, K., Miller, J. B., Bruhwiler, L. M. P., Petron, G., Hirsch, A. I., Worthy, D. E. J., van der Werf, G. R., Randerson, J. T., Wennberg, P. O., Krol, M. C., and Tans, P. P.: An atmospheric perspective on North American carbon dioxide exchange: CarbonTracker, P. Natl. Acad. Sci. USA, 104, 18925–18930, https://doi.org/10.1073/pnas.0708986104, 2007.

Pollard, D. F., Robinson, J., and Shiona, H.: TCCON data from Lauder (NZ), Release GGG2014.R0, TCCON data archive, CaltechDATA [data set], https://doi.org/10.14291/TCCON.GGG2014.LAUDER03.R0, 2019.

Rödenbeck, C.: Estimating CO$_2$ sources and sinks from atmospheric mixing ratio measurements using a global inversion of atmospheric transport, Tech. rep., Max Planck Institute for Biogeochemistry, Jena, Germany, 2005.

Rödenbeck, C., Zaehle, S., Keeling, R., and Heimann, M.: How does the terrestrial carbon exchange respond to interannual climatic variations? A quantification based on atmospheric CO$_2$ data, Biogeosciences, 15, 2481–2498, https://doi.org/10.5194/bg-15-2481-2018, 2018.

Rodgers, C. D.: Inverse Methods for Atmospheric Sounding: Theory and Practice, World Scientific, Singapore, ISBN 9814498688, 2000.

Schneising, O., Buchwitz, M., Reuter, M., Bovensmann, H., Burrows, J. P., Borsdorff, T., Deutscher, N. M., Feist, D. G., Griffith, D. W. T., Hase, F., Hermans, C., Iraci, L. T., Kivi, R., Landgraf, J., Morino, I., Notholt, J., Petri, C., Pollard, D. F., Roche, S., Shiomi, K., Strong, K., Sussmann, R., Velazco, V. A., Warneke, T., and Wunch, D.: A scientific algorithm to simultaneously retrieve carbon monoxide and methane from TROPOMI onboard Sentinel-5 Precursor, Atmos. Meas. Tech., 12, 6771–6802, https://doi.org/10.5194/amt-12-6771-2019, 2019.

Shiomi, K., Kawakami, S., Ohyama, H., Arai, K., Okumura, H., Taura, C., Fukamachi, T., and Sakashita, M.: TCCON data from Saga, Japan, Release GGG2014R0, TCCON data archive, CaltechDATA, https://doi.org/10.14291/tccon.ggg2014.saga01.R0/1149283, 2014.

Sussmann, R. and Rettinger, M.: TCCON data from Garmisch (DE), Release GGG2014.R2, TCCON data archive, CaltechDATA [data set], https://doi.org/10.14291/TCCON.GGG2014.GARMISCH01.R2, 2018.

Taylor, T. E., O'Dell, C. W., O'Brien, D. M., Kikuchi, N., Yokota, T., Nakajima, T. Y., Ishida, H., Crisp, D., and Nakajima, T.: Comparison of cloud-screening methods applied to GOSAT near-infrared spectra, IEEE T. Geosci. Remote, 50, 295–309, https://doi.org/10.1109/TGRS.2011.2160270, 2012.

Taylor, T. E., O'Dell, C. W., Frankenberg, C., Partain, P. T., Cronk, H. Q., Savtchenko, A., Nelson, R. R., Rosenthal, E. J., Chang, A. Y., Fisher, B., Osterman, G. B., Pollock, R. H., Crisp, D., Eldering, A., and Gunson, M. R.: Orbiting Carbon Observatory-2 (OCO-2) cloud screening algorithms: validation against collocated MODIS and CALIOP data, Atmos. Meas. Tech., 9, 973–989, https://doi.org/10.5194/amt-9-973-2016, 2016.

Taylor, T. E., Eldering, A., Merrelli, A., Kiel, M., Somkuti, P., Cheng, C., Rosenberg, R., Fisher, B., Crisp, D., Basilio, R. and Bennett, M.: OCO-3 early mission operations and initial (vEarly) XCO$_2$ and SIF retrievals, Remote Sens. Environ., 251, 112032, https://doi.org/10.1016/j.rse.2020.112032, 2020.

Taylor, T. E., O'Dell, C. W., Baker, D., Bruegge, C., Chang, A., Chapsky, L., Chatterjee, A., Cheng, C., Chevallier, F., Crisp, D., Dang, L., Drouin, B., Eldering, A., Feng, L., Fisher, B., Fu, D., Gunson, M., Haemmerle, V., Keller, G. R., Kiel, M., Kuai, L., Kurosu, T., Lambert, A., Laughner, J., Lee, R., Liu, J., Mandrake, L., Marchetti, Y., McGarragh, G., Merrelli, A., Nelson, R. R., Osterman, G., Oyafuso, F., Palmer, P. I., Payne, V. H., Rosenberg, R., Somkuti, P., Spiers, G., To, C., Weir, B., Wennberg, P. O., Yu, S., and Zong, J.: Evaluating the consistency between OCO-2 and OCO-3 XCO$_2$ estimates derived from the NASA ACOS version 10 retrieval algorithm, Atmos. Meas. Tech., 16, 3173–3209, https://doi.org/10.5194/amt-16-3173-2023, 2023.

Té, Y., Jeseck, P., and Janssen, C.: TCCON data from Paris (FR), Release GGG2014.R0, TCCON data archive, CaltechDATA [data set], https://doi.org/10.14291/tccon.ggg2014.paris01.R0/1149279, 2014.

Warneke, T., Messerschmidt, J., Notholt, J., Weinzierl, C., Deutscher, N. M., Petri, C., and Grupe, P.: TCCON data from Orléans (FR), Release GGG2014.R1, TCCON data archive, CaltechDATA [data set], https://doi.org/10.14291/TCCON.GGG2014.ORLEANS01.R1, 2019.

Wennberg, P. O., Wunch, D., Roehl, C., Blavier, J.-F., Toon, G. C., Allen, N., Dowell, P., Teske, K., Martin, C., and Martin., J.: TCCON data from Lamont (US), Release GGG2014R1, TCCON data archive, CaltechDATA [data set], https://doi.org/10.14291/tccon.ggg2014.lamont01.R1/1255070, 2016.

Wennberg, P. O., Roehl, C. M., Blavier, J.-F., Wunch, D., and Allen, N. T.: TCCON data from Jet Propulsion Laboratory (US), 2011, Release GGG2014.R1, TCCON data archive, CaltechDATA [data set], https://doi.org/10.14291/TCCON.GGG2014.JPL02.R1/1330096, 2017a.

Wennberg, P. O., Roehl, C., Wunch, D., Toon, G. C., Blavier, J.-F., Washenfelder, R. A., Keppel-Aleks, G., Allen, N., and Ayers, J.: TCCON data from Park Falls (US), Release GGG2014R1, TCCON data archive, CaltechDATA [data set], https://doi.org/10.14291/TCCON.GGG2014.PARKFALLS01.R1, 2017b.

Worden, J. R., Doran, G., Kulawik, S., Eldering, A., Crisp, D., Frankenberg, C., O'Dell, C., and Bowman, K.: Evaluation and attribution of OCO-2 XCO$_2$ uncertainties, Atmos. Meas. Tech., 10, 2759–2771, https://doi.org/10.5194/amt-10-2759-2017, 2017.

Wunch, D., Toon, G. C., Wennberg, P. O., Wofsy, S. C., Stephens, B. B., Fischer, M. L., Uchino, O., Abshire, J. B., Bernath, P., Biraud, S. C., Blavier, J.-F. L., Boone, C., Bowman, K. P., Browell, E. V., Campos, T., Connor, B. J., Daube, B. C., Deutscher, N. M., Diao, M., Elkins, J. W., Gerbig, C., Gottlieb, E., Griffith, D. W. T., Hurst, D. F., Jiménez, R., Keppel-Aleks, G., Kort, E. A., Macatangay, R., Machida, T., Matsueda, H., Moore, F., Morino, I., Park, S., Robinson, J., Roehl, C. M., Sawa, Y., Sherlock, V., Sweeney, C., Tanaka, T., and Zondlo, M. A.: Calibration of the Total Carbon Column Observing Network using aircraft profile data, Atmos. Meas. Tech., 3, 1351–1362, https://doi.org/10.5194/amt-3-1351-2010, 2010.

Wunch, D., Wennberg, P. O., Toon, G. C., Connor, B. J., Fisher, B., Osterman, G. B., Frankenberg, C., Mandrake, L., O'Dell, C., Ahonen, P., Biraud, S. C., Castano, R., Cressie, N., Crisp, D., Deutscher, N. M., Eldering, A., Fisher, M. L., Griffith, D. W. T., Gunson, M., Heikkinen, P., Keppel-Aleks, G., Kyrö, E., Lindenmaier, R., Macatangay, R., Mendonca, J., Messer-schmidt, J., Miller, C. E., Morino, I., Notholt, J., Oyafuso, F. A., Rettinger, M., Robinson, J., Roehl, C. M., Salawitch, R. J., Sherlock, V., Strong, K., Sussmann, R., Tanaka, T., Thompson, D. R., Uchino, O., Warneke, T., and Wofsy, S. C.: A method for evaluating bias in global measurements of CO$_2$ total columns from space, Atmos. Chem. Phys., 11, 12317–12337, https://doi.org/10.5194/acp-11-12317-2011, 2011.

Wunch, D., Wennberg, P. O., Osterman, G., Fisher, B., Naylor, B., Roehl, C. M., O'Dell, C., Mandrake, L., Viatte, C., Kiel, M., Griffith, D. W. T., Deutscher, N. M., Velazco, V. A., Notholt, J., Warneke, T., Petri, C., De Maziere, M., Sha, M. K., Sussmann, R., Rettinger, M., Pollard, D., Robinson, J., Morino, I., Uchino, O., Hase, F., Blumenstock, T., Feist, D. G., Arnold, S. G., Strong, K., Mendonca, J., Kivi, R., Heikkinen, P., Iraci, L., Podolske, J., Hillyard, P. W., Kawakami, S., Dubey, M. K., Parker, H. A., Sepulveda, E., García, O. E., Te, Y., Jeseck, P., Gunson, M. R., Crisp, D., and Eldering, A.: Comparisons of the Orbiting Carbon Observatory-2 (OCO-2) X_{CO_2} measurements with TCCON, Atmos. Meas. Tech., 10, 2209–2238, https://doi.org/10.5194/amt-10-2209-2017, 2017.